

Development of a Method for Genetic Optimization of Aerodynamic Devices

by

Raphael Lace Aranha

A thesis submitted to the
School of Graduate and Postdoctoral Studies in partial
fulfilment of the requirements for the degree of

Master of Applied Science in Mechanical Engineering

Faculty of Engineering and Applied Science

University of Ontario Institute of Technology (Ontario Tech University)

Oshawa, Ontario, Canada

June 2021

© Raphael Lace Aranha, 2021

THESIS EXAMINATION INFORMATION

Submitted by: **Raphael Lace Aranha**

Master of Applied Science in Mechanical Engineering

Thesis title: Development of a Method for Genetic Optimization of Aerodynamic Devices

An oral defence of this thesis took place on June 11, 2021, in front of the following examining committee:

Examining Committee:

Chair of Examining Committee	Sayyed Ali Hosseini
Examining Committee Member	Haoxiang Lang
Thesis Examiner	Amirkianoosh Kiani, Ontario Tech University / FEAS

The above committee determined that the thesis is acceptable in form and content and that a satisfactory knowledge of the field covered by the thesis was demonstrated by the candidate during an oral examination. A signed copy of the Certificate of Approval is available from the School of Graduate and Postdoctoral Studies.

ABSTRACT

Driving stability, fuel efficiency and soiling reduction are important for modern vehicles. This thesis has developed a novel method for genetic optimization of aerodynamic devices for road vehicle applications with the objective of minimizing drag and lift. The method involves the integration of genetic algorithms, B-spline shape optimization and computational fluid dynamic using OpenFOAM. The method can generate multiple devices in a single run. It allows the user to decide the objective functions and number of devices to be generated. The method was successfully applied to generate unique device geometries based on the Ahmed body by optimizing the top flap device and bottom diffuser, as well as the combination of the two devices. In addition, advanced vortex identification techniques were applied to the novel aerodynamic devices developed. The study provided physical insight into the drag and lift reduction as well as soiling mitigation mechanisms by the new devices.

Keywords: Genetic algorithm, shape optimization; CFD, OpenFOAM, Ahmed body; drag reduction; lift reduction; soiling reduction.

AUTHOR'S DECLARATION

I hereby declare that this thesis consists of original work of which I have authored. This is a true copy of the thesis, including any required final revisions, as accepted by my examiners.

I authorize University of Ontario Institute of Technology (Ontario Tech University) to lend this thesis to other institutions or individuals for the purpose of scholarly research. I further authorize University of Ontario Institute of Technology (Ontario Tech University) to reproduce this thesis by photocopying or by other means, in total or in part, at the request of other institutions or individuals for the purpose of scholarly research. I understand that my thesis will be made electronically available to the public.

Raphael Lace

Raphael Lace Aranha

STATEMENT OF CONTRIBUTIONS

I hereby certify that I am the sole author of this thesis, and a part of this thesis has been submitted for publication in a conference. I have used standard referencing practices to acknowledge ideas, research techniques, or other materials that belong to others. Furthermore, I hereby certify that I am the sole source of the creative works and/or inventive knowledge described in this thesis.

Part of the work described in Chapter 4 has been accepted for publication in a conference paper as:

R. Aranha, M. Agelin-Chaab and A. Alcon “Design of Aerodynamic Devices Using Genetic Optimization”, *Proceedings of the Canadian Society for Mechanical Engineering International Congress 2021*.

ACKNOWLEDGEMENTS

I would like to acknowledge my family, who supports me emotionally and financially during all this time of my master degree. They supported me and did not let me give up even though I want it so many times. Without their support, I would have given up long ago. I also would like to acknowledge Dr. Martin Agelin-Chaab that also played a bigger part in the conclusion of my degree. During this pandemic, he was also supporting me and helping me to complete my work. Without his support, this research would not be possible. Lastly, I would like to thank God that has been caring for me during these times, giving me insight and inspiration to achieve what I have done and also giving me strength. I also would like to thank especially Pedro Manuel and Giannina Bianchi, who helped me having access to Triton super computer. Without them obtaining the results would not be possible

TABLE OF CONTENTS

Abstract	ii
Author’s Declaration	iii
Statement of Contributions.....	iv
Acknowledgements	v
Table of Contents.....	vi
List of Tables.....	viii
List of Figures	ix
List of Abbreviations and Symbols	xi
Chapter 1 Introduction.....	1
1.1 Background	1
1.2 Objective	3
1.3 Thesis Structure.....	3
Chapter 2 Literature Review	4
2.1 Aerodynamic Devices for Road Vehicles	4
2.2 Shape Optimization of Ground Vehicles.....	6
2.3 Vortex Identification Techniques	9
2.4 Soiling Mitigation	10
2.5 Gaps in the Literature.....	13
Chapter 3 Methodology.....	14
3.1 Numerical Simulation.....	14
3.1.1 Calibration of the simulation.....	15
3.1.2 Inlet boundary conditions	15
3.1.3 Wall functions	16
3.1.4 Finite volume schemes.....	17
3.1.5 Mesh generation and model selection.....	18
3.1.6 Mesh independence test and validation	20
3.2 NSGA-II.....	23
3.2.1 Offspring and selection.....	23

3.2.2	<i>Crossover and mutation</i>	24
3.2.3	<i>Benchmarking the algorithm</i>	24
3.3	Quantification of the Wake	26
3.4	Geometry Generation Using B-spline	30
3.5	Integration of NSGA-II, B-spline and OpenFOAM.....	33
Chapter 4	Results and Discussion	34
4.1	Implementation of the Proposed Method	34
4.2	Flap Optimization for Drag and Lift	35
4.3	Diffuser Optimization for Drag and Lift	40
4.4	Combined Flap and Diffuser Optimization for Drag and Lift.....	45
4.5	Flap Optimization for Drag and Soiling.....	50
Chapter 5	Concluding Remarks	55
5.1	Conclusion.....	55
5.2	Contribution	56
5.3	Future Work	56
References	58

LIST OF TABLES

CHAPTER 3

Table 3.1 Inlet conditions	16
Table 3.2 Boundary wall conditions	17
Table 3.3 Various schemes and the corresponding methods	18
Table 3.4 Experimental results from literature vs numerical (present study)	22
Table 3.5 Results of the recirculation zone quantification.....	30

CHAPTER 4

Table 4.1 Drag and lift coefficients for the selected flap geometry in Figure 4.2(d).....	36
Table 4.2 Drag and lift coefficients for the selected diffuser geometry in Figure 4.9(a).....	41
Table 4.3 Drag and lift coefficients for the selected flap geometry in Figure 4.16(a).....	46
Table 4.4 Drag coefficient and recirculation volume for the selected flap geometry in Figure 4.23(a)	51

LIST OF FIGURES

CHAPTER 2

Figure 2.1 Wake region of the Ahmed body.....12

CHAPTER 3

Figure 3.1 The Ahmed body in schematic with dimensions, where α is the slant angle [78] (a), and a CAD model with $\alpha = 35^\circ$ in the present study (b).....18

Figure 3.2 Mesh of the Ahmed body with 35° slant angle.....19

Figure 3.3 Grid independence test and comparison of numerical and experimental errors.20

Figure 3.4 Comparison of experimental data and simulation results. (a) Streamwise mean velocity, (b) transverse mean velocity, and (c) turbulence kinetic energy profiles.....21

Figure 3.5 Variation of simulation time step with (a) residual and (b) drag coefficient.....23

Figure 3.6 NSGA convergence test for f_2 vs f_1 as in Equations (3.7) and (3.8).25

Figure 3.7 Breakdown of (a) element. (b) Element division and (c) sub-element.27

Figure 3.8 Vectorial distribution of the subelement28

Figure 3.9 Base break down of the subelement. (a) Entire surface of the subelements with division. (b) Surface of lower subelement.....29

Figure 3.10 Recirculation zone captured.....29

Figure 3.11 Surface generations. (a) Diffuser surface and (b) flap surface31

Figure 3.12 Full Ahmed body with a flap and a diffuser.....32

Figure 3.13 Flowchart of the B-spline, NSGA-II and OpenFOAM integration. (a) Whole algorithm flow chart and (b) evaluation of each individual member of the population flow chart33

CHAPTER 4

Figure 4.1 Progression of the solutions with generations for the optimization of (a) flap for drag and lift (b) diffuser for drag and lift (c) combined flap and diffuser for drag and lift (d) flap for drag and soiling.....35

Figure 4.2 Samples of the result of the flap optimization for drag and lift.....36

Figure 4.3 Pressure contours for (a) baseline and (b) optimized flap37

Figure 4.4 Velocity magnitude for (a) baseline and (b) optimized flap.....38

Figure 4.5 Contour plots for vorticity $\omega_x = 200/s$ on x -component for (a) baseline and (b) optimized flap39

Figure 4.6 Contour plots for helicity $H = 7500m/s^2$ for (a) baseline and (b) optimized flap39

Figure 4.7 Contour plots for Q -criterion, where $Q/U_{ref}=150$ for (a) baseline and (b) optimized flap, where U_{ref} is the inlet velocity40

Figure 4.8 Contour plots for velocity magnitude for the y - and z -components for (a) baseline and (b) optimized flap40

Figure 4.9 Samples of the result of the diffuser optimization for drag and lift.....41

Figure 4.10 Pressure contours for (a) baseline and (b) optimized diffuser43

Figure 4.11 Velocity magnitude for (a) baseline and (b) optimized diffuser.....	43
Figure 4.12 Contour plots for vorticity $\omega_x = 200/s$ on x -component for (a) baseline and (b) optimized diffuser	44
Figure 4.13 Contour plots for helicity $H = 7500m/s^2$ for (a) baseline and (b) optimized diffuser	44
Figure 4.14 Contour plots for Q -criterion, where $Q/U_{ref}=150$ for (a) baseline and (b) optimized diffuser.....	44
Figure 4.15 Contour plots for velocity magnitude considering y - and z - components for (a) baseline and (b) optimized diffuser.....	45
Figure 4.16 Samples of the result of the flap and diffuser optimization considering drag and lift where (a), (c) and (e) are the upper view and (b), (d) and (f) are the lower view of each sample.....	46
Figure 4.17 Pressure contours for (a) baseline and (b) optimized flap and diffuser	47
Figure 4.18 Velocity magnitude for (a) baseline and (b) optimized flap and diffuser.....	48
Figure 4.19 Contour plots for vorticity $\omega_x = 200/s$ on x -component for (a) baseline and (b) optimized flap and diffuser	48
Figure 4.20 Contour plots for helicity $H = 7500m/s^2$ for (a) baseline and (b) optimized flap and diffuser	48
Figure 4.21 Contour plots for Q -criterion, where $Q/U_{ref} = 150$ for (a) baseline and (b) optimized flap and diffuser ..	49
Figure 4.22 Velocity magnitude considering y - and z -components for (a) baseline and (b) optimized flap and diffuser	49
Figure 4.23 Samples of the result of the flap optimization considering drag and recirculation volume.....	50
Figure 4.24 Pressure contours for (a) baseline and (b) optimized flap	51
Figure 4.25 Recirculation zone for (a) baseline and (b) optimized flap	52
Figure 4.26 Contour plots for vorticity $\omega_x = 200/s$ on x -component for (a) baseline and (b) optimized flap	52
Figure 4.27 Contour plots for helicity $H = 7500m/s^2$ on x -component for (a) baseline and (b) optimized flap.....	52
Figure 4.28 Contour plots for Q -criterion, where $Q/U_{ref}=150$ for (a) baseline and (b) optimized flap.....	53
Figure 4.29 Velocity magnitude considering y - and z -components for (a) baseline and (b) optimized flap.....	53

LIST OF ABBREVIATIONS AND SYMBOLS

C_d	Drag coefficient
C_l	Lift coefficient
D_{ij}	Gradient tensor
A_{ij}	Symmetric tensor
B_{ij}	Skew-symmetric tensor
NSGA-II	<i>elitist</i> Non-dominated sorting genetic algorithm
\bar{u}	Average velocity
\bar{p}	Average pressure
ρ	Density
ν_{eff}	Effective viscosity
ν_t	Turbulent viscosity
ν_r	Viscosity ratio
ν	Viscosity
x_i	Spatial coordinate with respect of i direction
κ	Turbulent kinetic energy
ω	Specific rate of dissipation
U	Inlet velocity
I	Turbulent intensity
∇	Gradient
ΔV	Volume of mesh element
S	Surface area of one mesh element faces
h	Hight of sub-element

P	Control points
T	Knot Vectors
$\vec{\omega}$	Vorticity
\vec{U}	Velocity Vector
H	Helicity
ω_x	Vorticity on x -component
F_d	Drag force
F_l	Lift force

Chapter 1 Introduction

1.1 Background

The consumption of fossil fuels is a significant concern in modern society since it adversely impacts the environment [1]. Road transportation is one of the big consumers of fossil fuels and contributes significantly to greenhouse gas (GHG) emissions. For instance, the transportation industry alone contributes 30% of all GHG emissions in Canada [2]. Therefore, the pollution emitted by fossil fuels needs to be controlled and reduced. An effective way to do this is to reduce aerodynamic drag on ground vehicles [1,3-4]. It is well known that 80% of the drag is directly connected to the vehicle's geometry, and 50% of the fuel consumption is due to aerodynamic drag [3]. Therefore lowering drag is excellent for the environment. However, drag is not the only important feature in ground vehicles. Controlling lift, especially at high speeds, is also necessary to maintain the driver's safety [1]. High lift forces on a road vehicle do not provide good instability and can be dangerous to drivers. Also, for modern road vehicles, soiling reduction is of importance for operations [5-6]. This is more critical for self-driving vehicles which need to keep a clear vision for navigation.

One method of aerodynamic control is by using aerodynamic devices. They are attractive and more commonly employed because changing the entire vehicle's shape is more difficult and expensive [7]. It is much easier for vehicle owners to accessorize their vehicles using add-on devices. These aerodynamic devices can be divided into two categories, passive and active. Active devices are the ones that belong to the category of intelligent control [8], while passive devices do not have any control approach. However, passive devices are generally simpler and cheaper to employ because they do not require energy input to function. Therefore, passive devices were considered in this study.

In order to take maximum advantage of the design of a device, it is necessary to take an in-depth look at the shape optimization methodologies. There are many optimization methodologies, such as linear programming, Lagrange methods, adjoint methods, and evolutionary algorithms. Adjoint optimization is relatively recent in OpenFOAM and offers reasonable computational cost [9], since they only scale with the number of objective functions, such as drag and lift, and not with design variables. However, they are not as versatile as evolutionary algorithms, which can solve an unconventional problem, including combinatorial problems like the travel salesman problem [10], for which gradient methods, such as adjoint optimization, are not suitable [11]. Since this study's final goal is to implement a combinatorial problem to be solved with various devices model, the evolutionary algorithm is appropriate for this case.

There is not much research in the literature on developing methodologies for road vehicle shape optimization. Most of the research about ground vehicles was very simple, like boat tail optimization [12], which considered simple design variables and a single objective. There is also truck optimization, which simplified the problem like this author [13], using two-dimensional (2-D) simulation or other research [14] that only considered the layout but no computational fluid dynamics (CFD) simulation. There are also researchers who only test the design variables without any algorithm [15-18]. The most complex cases were related to nose optimization, where the author used 3D optimization by employing breezier curves and artificial neural networks [19]; however, none of them was related to devices with multiple objectives. Therefore, it was decided to develop a methodology that will automatically work with any aerodynamic devices and parts of the cars based on some user inputs.

In this thesis, the evolutionary algorithm is combined with computational fluid dynamics. This is because the objectives of aerodynamic optimization, such as drag and downforce, are

mostly contradictory. The evolutionary algorithm is a methodology that can keep the balance between them [20]. The *elitist* Non-dominated sorting genetic algorithm (NSGA-II) was selected for this study because it can handle multiple objective functions. Further, previous works have proved its applicability and efficiency [20].

1.2 Objective

The main objective of this study is to develop a methodology and algorithm to generate optimized aerodynamic devices based on a set of aerodynamic conditions in order to improve the aerodynamic performance of road vehicles. The specific objectives are as follows:

- Propose and develop a methodology to optimize aerodynamic devices for drag, lift, and soiling reduction.
- Apply the proposed method to develop new aerodynamic devices to reduce drag and increase downforce using a generic vehicle model such as the Ahmed body.
- Conduct detailed numerical analysis to evaluate the performance of the new aerodynamic devices

1.3 Thesis Structure

This thesis is organized into five chapters, including the current chapter. Chapter 2 highlights the critical literature on automotive aerodynamics and the control of aerodynamic forces. Chapter 3 details the methodology employed in this thesis. In Chapter 4, the results from this work are presented and discussed. Finally, Chapter 5 presents the conclusions of the study and provides recommendations for future work.

Chapter 2 Literature Review

This chapter contains the literature review of important aspects of this thesis. It is necessary to review previous works to identify gaps in the literature that the work will attempt to fill. The chapter will, therefore, cover the following sections:

- Aerodynamic Devices for Road Vehicles
- Shape Optimization of Ground Vehicles
- Vortex Identification Techniques
- Soiling Mitigation
- Gaps in the Literature

2.1 Aerodynamic Devices for Road Vehicles

The application of aerodynamic devices is not only limited to road vehicles but all vehicles in general. One example of that is the vortex generators that are commonly used in aircraft. The advantages of external aerodynamic devices are that they do not require changing the vehicle's shape to increase aerodynamic performance [21]. The vortex generator is responsible for transporting energy into the boundary layer from the outer flow, delaying the separation [22-23]. The objective of the device can change depending on the application. It can be solely focused on reducing fuel consumption [3], improving the performance in a race [7,24], or increasing safety [8]. The shape of the device can also change, depending on the type of vehicle. The form of the device will depend on the purpose or initial geometry (car body). It is possible to observe by looking at race cars [7,24], road cars [25] and trucks [26-28] which can have different types of devices optimized for their geometries or purpose. The type and shape of the device can be unique.

They can be rear-wing like shown in this article [7], or they can be fin types, for race cars [24] even sliced diffusers. Even for the same vehicle category, the number of shapes possible, as shown by Nath [24] , tested different devices for trucks with minor changes. The number of devices can be infinite since the number of categories is vast, but each category's design is unique for each vehicle type. Therefore, designing a new device can be very time-consuming, and achieving optimality is not always guaranteed.

It has already been proved that flap devices provide good drag reduction in the Ahmed body [18]. Previous works [29] achieved up to 25% drag reduction in an Ahmed body using a rectangular flap. Also, Siddiqui [18] found that it could reduce drag on an Ahmed body using a rectangular flap with the optimal value of 10° inclination. Similarly, other researchers achieved reduction using rectangular plates [30] and flaps [31]. This confirms the efficiency of using flaps as passive drag control. However, all of these flaps reported in the literature were regular shapes. Altaf [32] employed different flap geometries (rectangular, triangular and elliptical) as devices for drag reduction on a long haul MAN TGX truck (by the German vehicle manufacturer MAN Truck & Bus). He found that the elliptical flap provides the best drag reduction. This confirms that it is possible to find even better drag and soiling reduction by optimizing the shape. Therefore, this thesis proposes to design a flap with multi-degrees of freedom to enhance downforce and drag reduction on the Ahmed body.

Besides, diffusers can be used as devices to improve a road vehicle's downforce and stability [33]. Some previous work attempts to design a diffuser for a race car by changing the diffuser angle [17]. Other works also proposed adding fences to further enhance the downforce [34-35]. Additionally, some researchers put a convex bump at the end of the diffuser to improve its effectiveness [33]. There is no established methodology in the literature to enhance diffuser

performance. Therefore, this thesis will propose a way to design a diffuser using a genetic algorithm and potentially combine it with a flap to extract maximum performance.

For the reasons above, the thesis proposes a methodology to design a combination of devices (flap and diffuser) for road vehicle application. However, the final goal of this work is not only to create a variety of flap and diffuser but to extend the methodology to multiple families of devices (fin, spoilers, vortex generators, etc.) and let the algorithm decide the best combination of these devices for an improved vehicle aerodynamic performance.

Many methods of optimization were already proposed. Salhan [36] conducted CFD simulations to investigate a number of aerodynamic devices on the MIRA fastback model. However, other studies performed tests on the aerodynamic devices in combinations [15-17] to check what combinations of devices have better performance. Further, some try to optimize a single device by changing some parameters. For example, Khosravi [27] tried to find the most optimal angle of a truck's reflector, whereas the diffuser angle of a race car was also investigated by Hassan [17]. As mentioned earlier, Siddiqui [18] also tested many angles of a flap to find the most optimal one to reduce drag on the Ahmed body. Although the above studies show improvement in the overall drag reduction or an increase in downforce, they cannot enhance their devices further because they are changing one variable at a time. To find better results, it is necessary to consider more variables that can change an aerodynamic device's overall design. By considering more variables, it is not feasible to manually test the results. Therefore, an algorithm is necessary.

2.2 Shape Optimization of Ground Vehicles

Investigating a large number of different combinations of variables in a parametric

approach is too costly and not practical. As a result, an optimization algorithm is necessary to implement more complex cases. One of the main problems with simulation and optimization is selecting a suitable algorithm [11]. There is no such thing as universal algorithm selection nor guidelines for that [11]. The main concerns to be kept in mind is the nature of the problem. In order to find better solutions, two practical methods for optimization can be selected for road vehicles, the adjoint method [37] and the evolutionary algorithm [12]. Gradient methods are not suitable for discontinuous problem [11]. Since the final goal is to implement a discontinuous problem, the adjoint method is not the right choice for this study. One other option is the metaheuristic approach. There are many types of algorithms for metaheuristics and many articles proposing modifications of the already existing ones. Luckily, there are many previous studies related to aerodynamics where genetic algorithms were used [12-13,19,38-47], which confirms the application of a genetic algorithm for aerodynamic applications. However, most of them are related to aerospace and wind turbine blade optimization.

Previous studies have already shown that genetic algorithm can be successfully applied to ground vehicles [12-13,19,46-47]. Muijl [12] used a hybrid genetic algorithm to optimize the boat tail using one objective function (drag) and three variables that are only the angle. The results showed that the algorithm is more effective if compared with the standard genetic algorithm, but his setup oversimplified the problem. However, it has only one objective function. Similarly, Doyle [13] used a genetic algorithm to optimize flap for a truck using cubic functions and one objective function, and four variables that are the control points. Although he reduced the drag by 50%, the problem was oversimplified into a two-dimensional simulation, but the flow around ground vehicles is strongly three-dimensional (3-D) in nature. In addition, Muñoz [19] performed a single objective optimization in a crosswind scenario for a rail train using a genetic algorithm

and the adjoint method and compared their performances. The results show that the genetic algorithm produced a better performance with a 9% reduction in the crosswind, while the adjoint method achieved only a 4% reduction. Although genetic algorithms are more expensive, the results show that they can overperform the adjoint methods. Similarly, Yu [47] and Yuan [46] also did optimization of the nose of the train using genetic algorithms. Yu [47] achieved a drag reduction of 4.2% and a weight reduction of 1.7%. On the other hand, Yuan [46] obtained a 6.7% drag reduction and a noise reduction of 8.34 decibels.

After analyzing these works, it can be observed that the choice of an appropriate algorithm is not an easy process. Muyl [12] used a hybrid genetic algorithm for optimizing a boat tail, Yu used the NSGA-II (*elitist* Non-dominated sorting genetic algorithm) [47], and Yuan used a modified version of the NSGA-II [46]. This confirms that researchers can use different versions of the algorithms depending on the peculiarity of their work. This makes it challenging to choose an algorithm. According to Yang [11], the choice of an algorithm is subjective and personal to the researcher. Since the present study's scope is multi-objective optimization, the NSGA-II algorithm was selected for this case because it has been proven reliable by previous studies [46-47]. NSGA-II is an effective algorithm that deals with multi-objective optimization. It is one of the most popular algorithms [48], and is based on non-dominated sorting, as indicated by its name NSGA-II. This algorithm will keep the function with better results (non-dominated) and better-crowded distance, maintaining the diversity of results. Even though NSGA-II is employed for this research, the algorithm is not the main scope here. It is part of future research to extend this methodology to other optimization algorithms, which will give the user the freedom to select from a variety of algorithms available.

2.3 Vortex Identification Techniques

There are many applications for vortex identification techniques as a postprocessing tool. Many works have been performed on vortex interaction with other physical responses. Some of them described drag and vortices [18,49-50], others make the connection between vortices and vibration [51-53]. Matsumoto [51] reviewed types of vortex generation and described their physical connection with the vibration responses of bluff bodies. He also provided a review of previous work done on vortex studies. Similarly, Leclercq [52] conducted a study connecting the vortex formation in a bluff body with noise production and provides good literature on previous works. He used experimental and numerical results to propose a model to explain the noise.

Also, Fitzpatrick [53] studied the noise generated by turbulence in tandem cylinders. Other researchers also pointed the connection between drag and vortex formation. Bearman [49] and Mizota [50] studied Karman vortices positions on a 2-D rectangular cylinder and the drag forces. They discovered that the closer the formation of vortices to the rear face, the stronger the forces. Unlike those works that only analyze 2-D bodies, Siddiqui [12] used vortex identification to explain the drag reduction device's physics on an Ahmed body. He discovered that using a 10° rectangular flap on an Ahmed body reduced the kinetic energy and the vortex radius, justifying the drag reduction. It was also observed that drag is reduced by reducing the longitudinal vortices' strength at the edges of the slant surface.

It is well known that the vortices do not have a proper mathematical definition [54], despite many people having a contrary view. However, mathematical methods are necessary to identify them. This work will present one of these methods to post-process the results obtained through optimization. It will deliver the second generations of vortex identification techniques, Q -criterion [55].

The Q -criterion use the velocity gradient tensor to identify their structures, so having a clear understanding of the tensor is essential. The mathematical formula of the tensor can be found in [54] and has the following definition:

$$D_{ij} = \frac{\partial u_i}{\partial x_j} \quad (2.1)$$

Where u_i is the velocity component of that direction, and x_j is a variable in the space. This tensor can be subdivided into two matrices that will be used for the Q -criterion [54] [55]. These matrices are the symmetric (A) and a skew-symmetric (B) that can be extracted from the tensor, and the formula is shown below [54-55]:

$$A_{ij} = \frac{1}{2} \left(\frac{\partial u_i}{\partial x_j} + \frac{\partial u_j}{\partial x_i} \right) \quad (2.2)$$

$$B_{ij} = \frac{1}{2} \left(\frac{\partial u_i}{\partial x_j} - \frac{\partial u_j}{\partial x_i} \right) \quad (2.3)$$

The Q -criterion formulas use the matrices above, and the formulas are shown below [54-55]:

$$Q = \frac{1}{2} (\|B\|^2 - \|A\|^2) \quad (2.4)$$

It is crucial to use vortex identification techniques to understand the physical mechanisms of the devices better.

2.4 Soiling Mitigation

Soiling mitigation is an essential feature for modern cars, especially for vehicles with

vision sensors for self-driving, where it is necessary to have a clear vision to ensure safety. As a result, it is good to have devices that will minimize soiling. To develop a methodology for soiling reduction, it is necessary to understand the mechanism of soiling clearly. There are three main sources of soiling: from the environment, other vehicles and self-soiling. The focus of this research is to reduce the rear self-contamination that is caused by self-soiling, especially the tyre spray [56]. The droplets emanated from the wheel to the vehicle wake, and recirculation makes them going back to contaminate the vehicle surface [56]. It can be concluded that the rear wake optimization is the most critical part for soiling mitigation.

Yoshida [57] was one of the first to perform a comprehensive study on soiling Lagrangian and Eulerian methods to estimate the contamination. However, their work was a simplification, and the flow solution was far from accurate. Since then, other researchers have done similar work. Roettger [58-59] used a time-averaged flow field to calculate the deposition on the vehicle's rear. Later, Paschkewitz [60-61] analyzed particle dispersion and found a significant difference between unsteady and steady solutions. He pointed out that Yoshida [57] was premature in his study when he mentions that there was no difference between unsteady and steady flows. The first calibrated tyre spray model was done by Kuthada [62], and it was further enhanced due to experimental results provided by Spruss [63]. The improved model was used by Gaylard [64] on a saloon car and a sports utility vehicle on CFD simulations for side and rear soiling. More recently, Jilesen [56] studied the soiling impact on the EV12 model with geometries modifications. He concluded that contamination is sensitive to the rear wheel and base wake interactions. The previous studies have shown that the interactions between the wakes cause soiling; an algorithm to reduce the recirculation size will be developed to try to minimize the advection of the particles into the rear wake region.

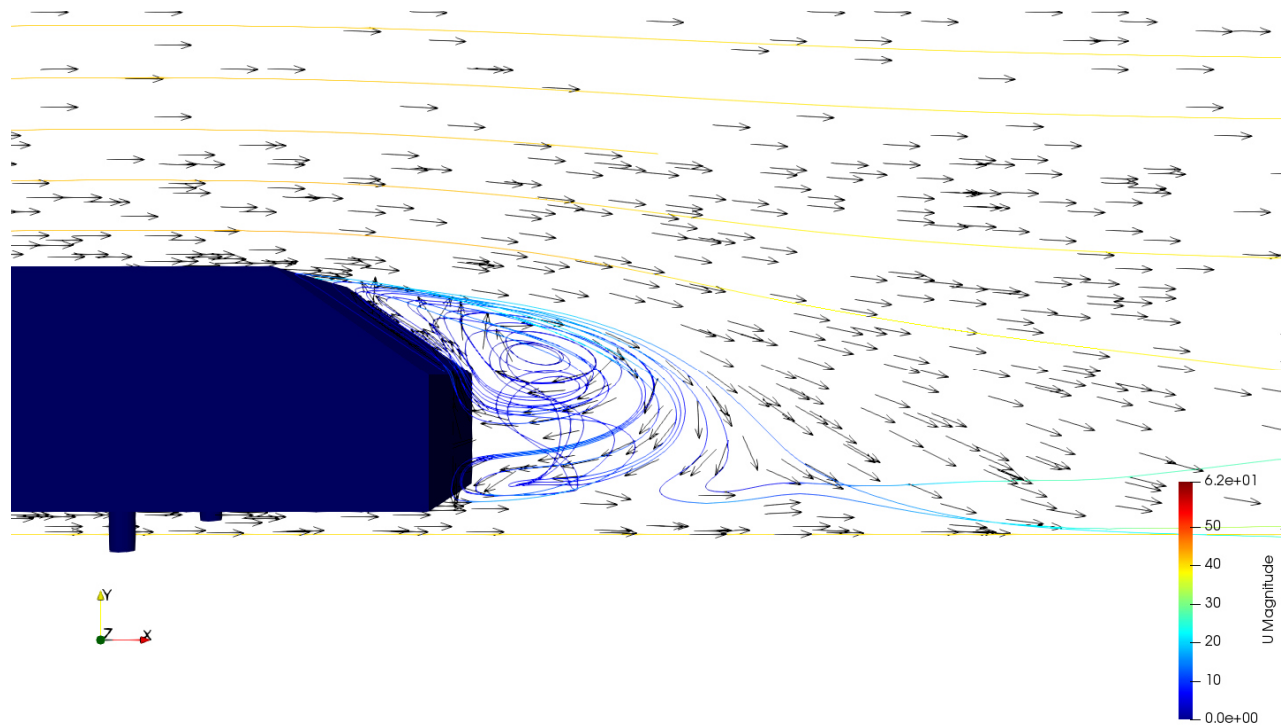


Figure 2.1 Wake region of the Ahmed body

For numerical approaches, the solvers employed are important. A homogenous solver could be used to reduce soiling. Some authors use steady solvers [58-59]. Others claim that the solution for steady and unsteady have significant differences [60-61], and it is known that steady solvers fail to recover the rear wake structure and pressure distribution, which are vital for this problem [56,66]. However, it is important to mention that using an unsteady solver is much more expensive, especially if it includes large Eddy simulation models. Thus, the problem will be simplified using a steady solver with Reynolds Averaged Navier-Stokes models to measure and reduce the recirculation zone. This reduction will minimize the interaction between the vehicle's rear and its wheel wake, resulting in soiling reduction.

2.5 Gaps in the Literature

From the literature review above, the following gaps can be identified:

- There is a lack of studies on the optimization of aerodynamic devices for soiling mitigation for ground vehicles.
- No other work considers using vortex identification techniques as an objective function when designing devices for ground vehicles.
- There is a lack of studies that consider using families of aerodynamic devices to optimize the performance of a road vehicle.
- There is no integrated methodology for optimal integration of multiple aerodynamic devices using a genetic algorithm.

Chapter 3 Methodology

This chapter is dedicated to the methodology. All the background used to solve and develop the methodology was reviewed in the previous chapter. It is necessary to have a deep knowledge of simulation and optimization to build the application and debug it. This chapter is divided into the following five main sections:

- Numerical simulation
- NSGA-II implementation
- Quantification of the wake region
- Geometry generation using B-spline
- Integration of NSGA-II, B-spline and OpenFOAM

3.1 Numerical Simulation

For this study, the objective functions are connected to the solution of the Navier-Stokes equations [67]. Without understanding these equations, it is not possible to develop further postprocessing, such as vortex identification techniques, or to calibrate the simulation properly. The Navier-Stokes equations are shown below [67] :

$$\frac{\partial \bar{u}_i}{\partial t} + \bar{u}_j \frac{\partial \bar{u}_i}{\partial x_j} = -\frac{1}{\rho} \frac{\partial \bar{p}}{\partial x_i} + \frac{\partial}{\partial x_j} \left([\nu_{eff}] \left(\frac{\partial \bar{u}_i}{\partial x_j} + \frac{\partial \bar{u}_j}{\partial x_i} \right) \right) \quad (3.1)$$

Where \bar{u} is the average velocity, \bar{p} the average pressure, ρ is the density and ν_{eff} is the effective viscosity.

In order to find a closer solution to reality, the CFD simulation was enhanced using turbulence models. One of the turbulence models chosen by this research was the Reynolds averaged Navier-Stokes (RANS), more specifically the κ - ω SST. Choosing the turbulence model

requires some consideration. It is well known that large eddies simulation(LES) models have better performance than RANS models [68-70]. However, they are extremely costly because they are transient models and also need a very fine mesh. This makes them an unreasonable choice to use with the optimization. Many authors claimed that the RANS model provides accurate enough results [67,71-72]. Furthermore, Siddiqui [18] argued that κ - ω SST models are good models for flow simulation around the Ahmed body. Also, Igali [73] has shown that they achieved the best results with the κ - ω SST model when compared with other turbulence models on Ahmed body simulation. Similarly, Tian [31] achieved promising results with the same turbulence model for flow simulation around the Ahmed body. Based on the above, the κ - ω SST model was employed for this study.

3.1.1 Calibration of the simulation

The simulation setup was divided into four main areas. Each one of the sections will explain how and why the setup was selected. This is necessary because OpenFoam, different from commercial software, need more input from the user. The following subsections will be discussed.

- Inlet boundary conditions
- Wall function
- Finite volume schemes
- Simulation/calibration results

3.1.2 Inlet boundary conditions

One problem with setting up a simulation in OpenFOAM is how to handle the boundaries and the schemes correctly. To properly set up the boundary conditions in the inlet, the ANSYS user manual [74] was used to copy the inlet function and use it in OpenFoam. Two formulas were

used to set up the inlet that can be found in the ANSYS manual [74] :

$$\kappa = \frac{3}{2} (U \cdot I)^2 \quad (3.2)$$

$$\omega = \frac{\kappa}{\nu \cdot \nu_r} \quad (3.3)$$

$$\nu_r = \frac{\nu_t}{\nu} \quad (3.4)$$

Where κ is the turbulent kinetic energy, ω specific rate of dissipation, U is the inlet velocity, I is turbulent intensity and ν_r is viscosity ratio.

The values of the variables can be found in the chart below. To calculate the boundaries, a user-defined code was made to run before the simulation, and this code automatically calculates the inlet velocity selected.

Table 3.1 Inlet conditions

Inlet	Outlet
I	1%
ν_r	10
ν_t	Calculated
U	40m/s

3.1.3 Wall functions

For these scenarios, wall functions were used to speed up the simulation. Even though the wall function provides good accuracy, they present problems in curved geometries and separation flows [75]. The problem is that the wall function works only for values of $30 \leq y^+ \leq 200$ or $y^+ \leq 5$ [75-76]. The simulation setup was made that most of the cells have this value, but the diffuser

and the flap have small parts which are not in this range. This is difficult to control since each run generates different flap and diffusers geometries. In conclusion, a little accuracy was lost in the process of speeding up the simulation, but most of the cells are still in the effective range for y^+ values. It is very difficult to get all the cells in the good range of y^+ because curved geometries are difficult to control the y^+ , as Bastian [75] reported.

The formula of the functions and the coefficients for the wall functions formulas can be found in a previous study [76].

Table 3.2 Boundary wall conditions

Bottom Wall	Moving wall
κ	kqRWallFunction
ω	omegaWallFunction
ν_t	nutkWallFunction
Ahmed Body	No-slip

3.1.4 Finite volume schemes

The finite volume schemes (FVschemes) were selected based on the OpenFOAM mesh (Hexahedral). The proper setup for the FVschemes can be found in the literature [75]. The procedure for using Gauss linear corrected as laplacian schemes were also followed, as suggested by the user manual for being the most accurate [75,77]. Since the OpenFOAM user manual recommends that the non-orthogonality not be higher than 70 degrees [77], 55 degrees as the maximum value for meshing was used in this case. The same was applied to the surface-normal gradient schemes. Since both Laplacian and surface-normal gradient schemes are connected, both of them have the same restriction of non-orthogonality be higher than 70 degrees, and both of them

used the corrected scheme, according to the OpenFOAM user manual [77].

Table 3.3 Various schemes and the corresponding methods

FvSchemes	Method
Gradient schemes	Gauss linear
$\nabla \cdot (\phi U)$	Gauss linearUpwindV grad(U);
$\nabla \cdot (\phi \kappa)$	Gauss upwind
$\nabla \cdot (\phi \omega)$	Gauss upwind
Laplacian Schemes	Gauss linear corrected
Surface-normal gradient schemes	Corrected

3.1.5 Mesh generation and model selection

The Ahmed body with a slant angle of 35° was selected for this study because it is one of the most commonly studied generic body and relatively well understood. There is also plenty of experimental data available in the open literature for validation. Figure 3.1 presents the schematic of the Ahmed body.

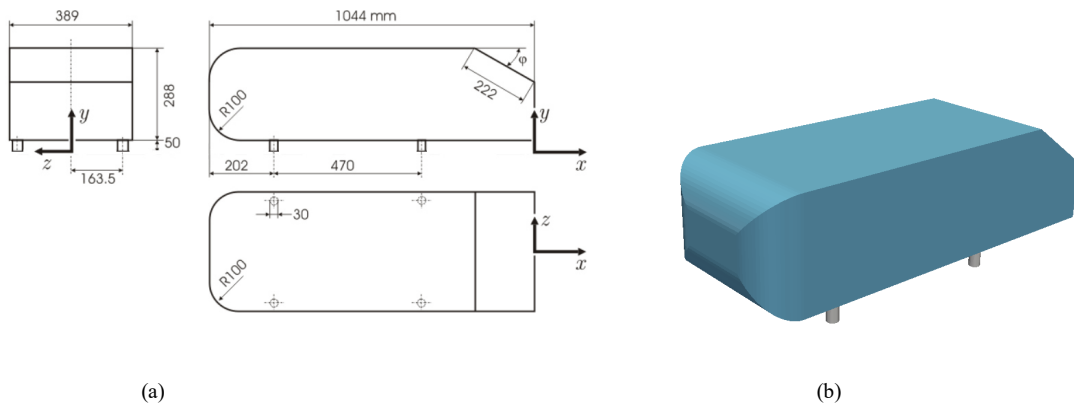


Figure 3.1 The Ahmed body in schematic with dimensions, where α is the slant angle [78] (a), and a CAD model with $\alpha = 35^\circ$ in the present study (b)

After the model is selected, the meshing is going to happen. The mesh application used was snappy hex mesh. Snappy hex mesh is a standard mesh tool in OpenFOAM which generates hexahedral mesh. The mesh specifications need to control not only the errors (non-orthogonality) in order to work with the finite volume schemes but also control y^+ to take the best advantage of wall functions. The mesh kept all the elements with a non-orthogonality below 55 degrees which helped the simulation to have accurate results and good convergence, and it is in agreement with finite volume schemes restrictions, as mentioned in section 3.1.4. The max element size selected was 50 mm, and the minimum was 6.25 mm on the refinement box. The refinement box had in total around 3 m in length, 0.5 m in height and 1 m in width. It was studied during the mesh independence that was the setup that produced the best values of y^+ and the ones with the most accurate drag coefficient values (Figure 3.2). The big majority of the values of y^+ were in the acceptable range, which is in agreement with the wall functions restrictions, as mentioned in section 3.1.3. The number of elements that this mesh produced was 15 million elements which, according to the mesh independence studies, was considered ideal.

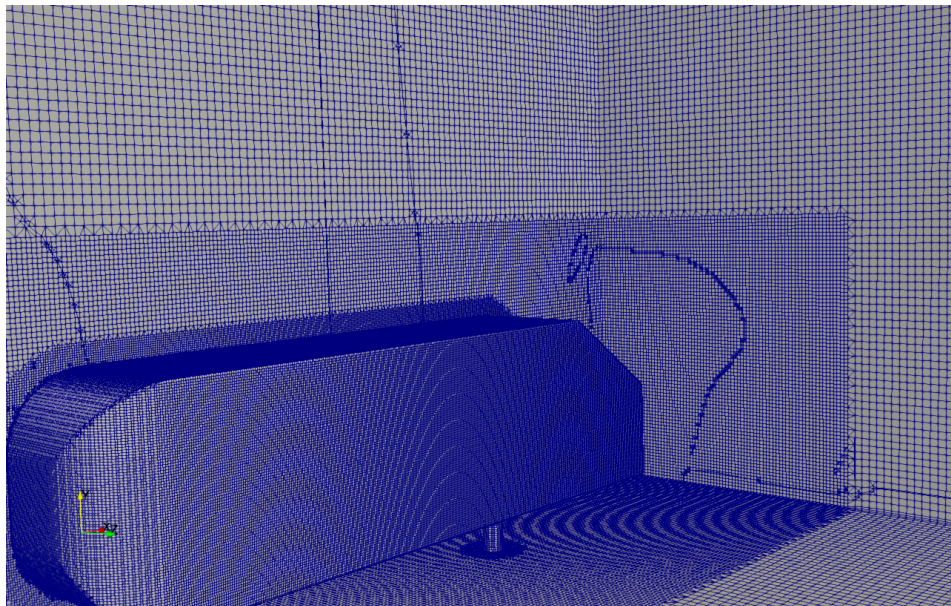


Figure 3.2 Mesh of the Ahmed body with 35° slant angle

3.1.6 Mesh independence test and validation

The first step of the calibration of the simulation is testing the mesh independence. The mesh independence is very important because it will show that the results are independent of the grid size. Figure 3.3 shows that at about 1.0×10^7 elements, the results start to not change much (becoming grid-independent) when compared with the experimental results. Figure 3.3 also illustrates that after this number of elements, all the simulation results produces less than 5% error when compared with experimental data (Ahmed body of 35° slant angle). This result is important because it can show the size of the grid that can be used to balance accuracy and speed. Basically, it was selected the grid size with the least number of elements which produce the least error in order to achieve both accuracy and improved simulation time. It was decided to use a grid size of around 1.5×10^7 in order to have a fast and accurate simulation.

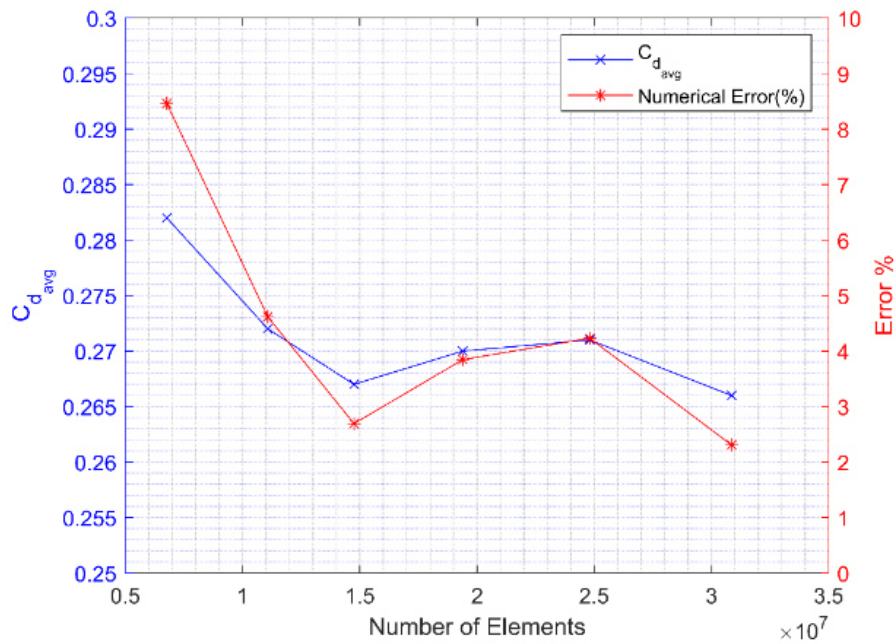


Figure 3.3 Grid independence test and comparison of numerical and experimental errors

To further validate the simulation results, available experimental data in the open literature was used [31,79-81]. Figure 3.4 illustrates how close the simulation profiles are to the experimental that is available online [79]. The model here presented is the Ahmed body of 35° slant angle. All data from Figure 3.4 is in good agreement with the experimental data.

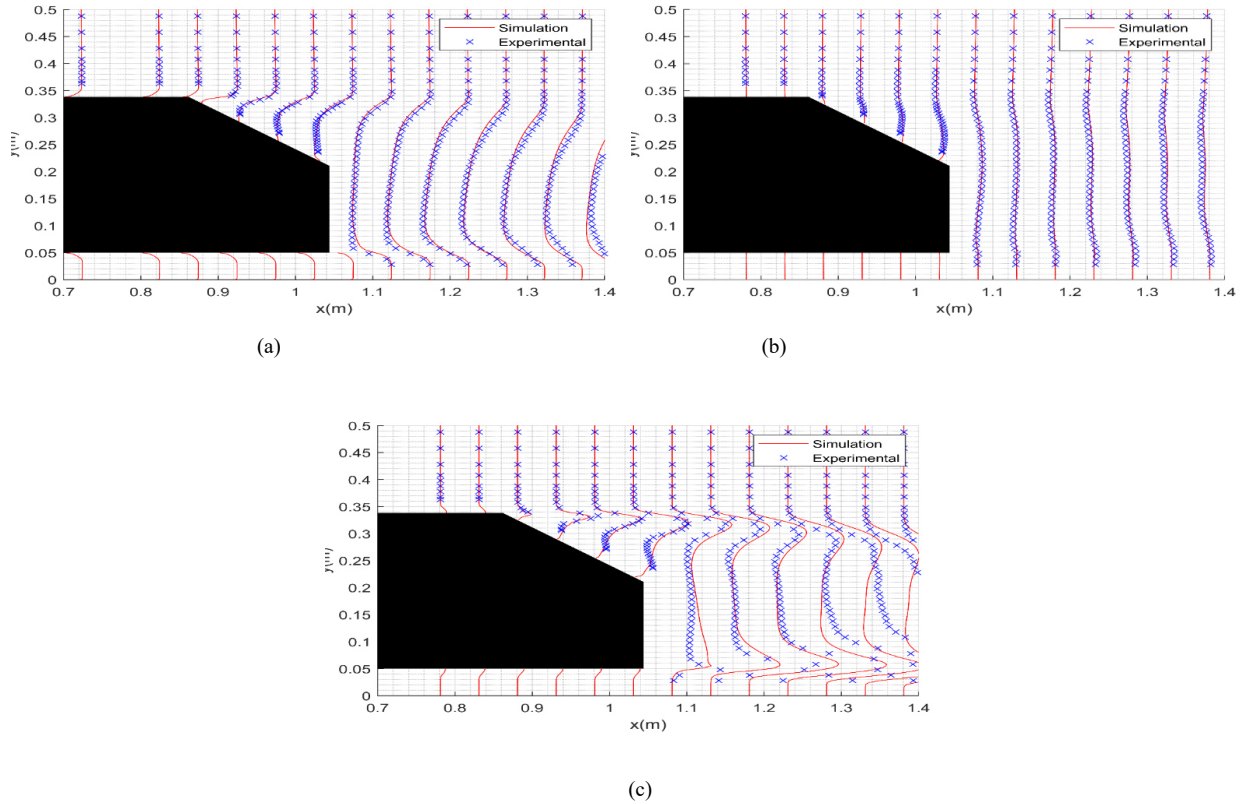


Figure 3.4 Comparison of experimental data and simulation results. (a) Streamwise mean velocity, (b) transverse mean velocity, and (c) turbulence kinetic energy profiles

Table 3.4 also compare the numerical results with the ones obtained through a wind tunnel [31,80-81]. These values were obtained by calculating the forces over the Ahmed body of 35 degrees slant angle. The wind tunnel used a velocity of 40 m/s (the same as in the simulation), the drag forces (which is the friction and pressure drag), and lift forces (caused by pressure) were measured and normalized into coefficients using the formulas of Equation (3.5) and Equation (3.6)

$$C_d = \frac{2F_d}{\rho V^2 A} \quad (3.5)$$

$$C_l = \frac{2F_l}{A\rho V^2} \quad (3.6)$$

Where F_l and F_d are the lift and drag forces, respectively, and A is the frontal surface of the Ahmed Body.

Table 3.4 Experimental results from literature vs numerical (present study)

	Experimental	Numerical
C_d	0.26 [31,80]	0.267
C_l	0.004 [81]	0.0154

From the results above (Table 3.4), it can be concluded that numerical results are in good agreement with the experimental data. All the errors in the simulation are below 5%, which is a good estimation for the results.

The last step of this analyzes to select the time step. Since in OpenFOAM, the time step is selected by the user, the user needs to adjust the time step until it converges. However, this is not possible since the optimization code will keep evaluating the individual members of the population automatically. Therefore, it is necessary to estimate the number of time steps necessary for convergence. To select the number of iterations, the residuals and the convergence of the aerodynamic forces were analyzed. By looking at the graphs below (Figure 3.5), it can be observed that after 800-900 iterations, both C_d and residuals are small and start to converge. So the number of iterations for the code was selected to be 1500.

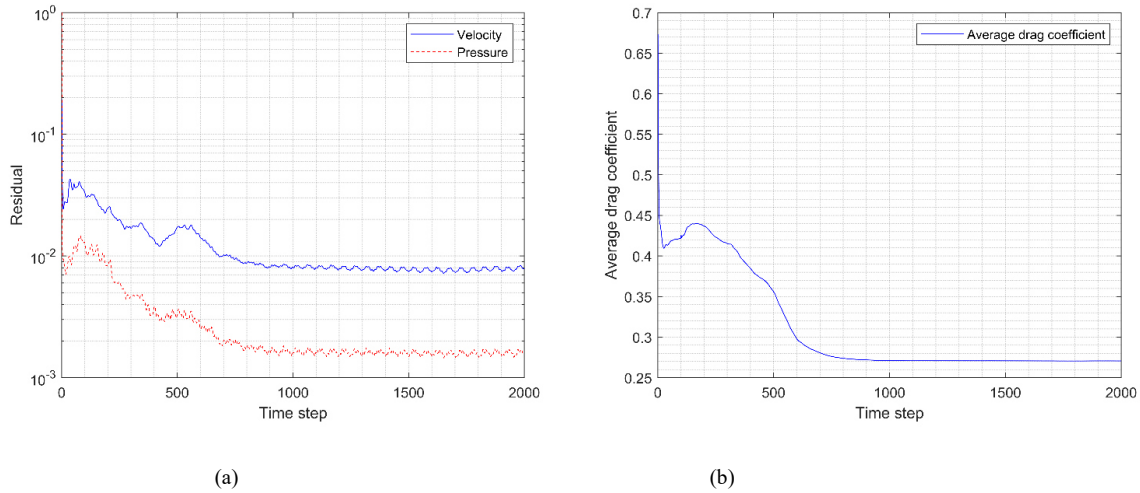


Figure 3.5 Variation of simulation time step with (a) residual and (b) drag coefficient

3.2 NSGA-II

The NSGA-II methodology was used to solve this problem since previous papers demonstrated its applicability for the multi-objective problem [82]. The idea is to use the non dominated solutions to make both offspring (tournament) and selection (need to be reformulated), as shown in the three subsections below [82-83].

- Offspring and selection
- Crossover and mutation
- Calibration

3.2.1 Offspring and selection

The critical step for offspring selection is the ranking of the population. The NSGA-II algorithm is based on the non dominated sorting. That is why ranking is an important criteria. The ranking is based on dominance, such that the less dominated has a better rank. The dominance criteria are based on the objective function. Suppose one individual member of the population

outperforms another individual member of the population in all the objective functions, the former dominates. This method is called dominance depth. For more information, the method can be found in the following references [83-84].

In order to generate offsprings, the tournament selection method was used. Two candidates are randomly selected from the population to participate in the tournament. The ones with better ranks and better-crowded distance win the competition and get in the mating pool. After that, they are generating offsprings until they reach the same size as the population. Lastly, the selection happens, and only the ones with ranks and better-crowded distance will survive.

3.2.2 Crossover and mutation

The crossover used for this code was uniform. The idea is the gene can swap with another chromosome based on a certain probability. The procedure for mutation is similar to the crossover. However, instead of swapping with another chromosome, it will just change one of the genes. This will happen randomly, and there is a certain amount of probability of happening in every reproduction.

3.2.3 Benchmarking the algorithm

To make sure that the NSGA-II code is working, a benchmark function with a known solution was selected for comparison. The ZTD1 function selected can be found in Yanga [85]. The probability of mutation was 3%, and the cross over was 85%. This setup was the same used to optimize the setup for OpenFoam. Seven bits of precision and 30-dimensional variables ($N = 30$ on Equation (3.9)) were selected. The equations for the benchmark function are listed below.

$$f_1(x) = x_1 \tag{3.7}$$

$$f_2(x) = g(x)|1 - \sqrt{1 - x_1/g(x)}| \quad (3.8)$$

$$g(x) = 1 + 9 \frac{\sum_{i=2}^N x_i}{n-1} \quad (3.9)$$

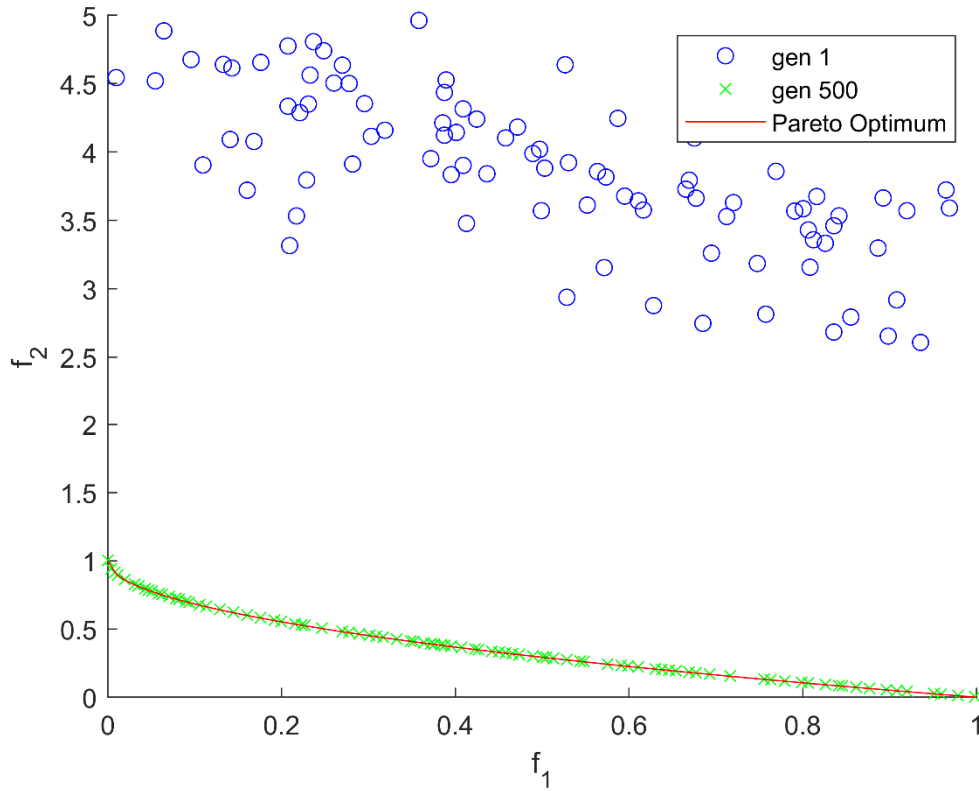


Figure 3.6 NSGA convergence test for f_2 vs f_1 as in Equations (3.7) and (3.8)

As illustrated in Figure 3.6, after 500 generations, the solution is similar to the Pareto Optimum. Therefore the NSGA-II algorithm can solve a generic problem in 30 dimensions with 7 bits of precision.

3.3 Quantification of the Wake

To use the recirculation zone as an objective function, the first step is to quantify the recirculation zone. The recirculation zone is one of the most critical factors in soiling, so to use that as an objective function, it is necessary to identify and quantify it. The criteria used is the total recirculation volume :

$$F = \sum_B \Delta V \quad (3.10)$$

Where B is the recirculation zone that is going to be applied numerical volume integration (F), and ΔV is the volume of each element.

In order to determine the size of the recirculation zone, it is necessary to find out which elements are inside of it. The recirculation zone is the place where the flow goes against the inlet velocity. So the criteria used to identify if the element is inside the recirculation zone or not is: $V_x < 0$. To calculate the volume of each element; each element was divided into subelements, and the volume of each element was then the sum of all subelements:

$$\Delta V = \sum \Delta V_{sub} \quad (3.11)$$

Now the criteria to divide into subelements was based on centre of gravity (CG). Since the shape of the element is unknown, this method was developed to use an algorithm to calculate all the elemental volumes. The only input used was the mesh information provided by Openfoam from the mesh generated. After reading the mesh, the algorithm re-builds every element and connects all the vertices to the centre of gravity of the element. This connection between the

vertices and the CG will generate a subelement that will be used to calculate the volume of the element.

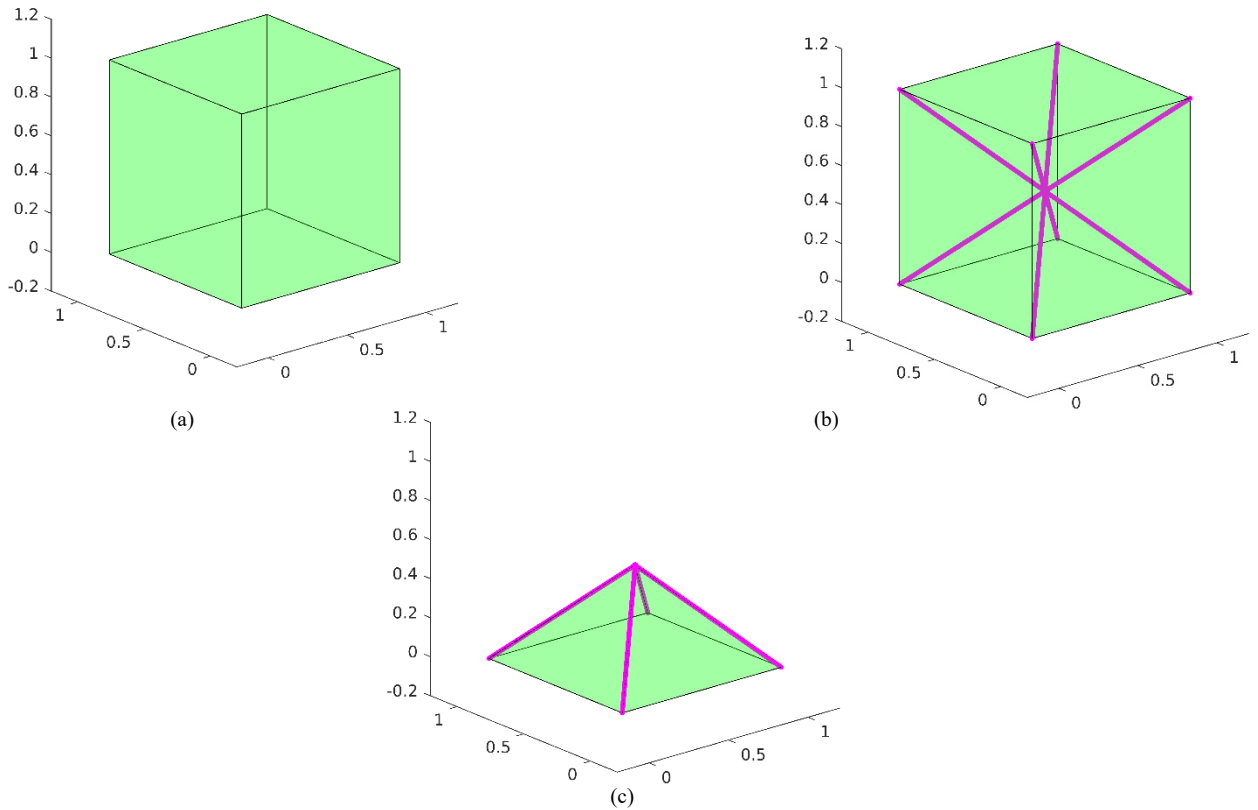


Figure 3.7 Breakdown of (a) element. (b) Element division and (c) sub-element

With this approach, the code can calculate all elements volumes as long as the element and the faces are convex. This is the main source of error. So long as the elements have good quality, the method is accurate. To calculate the volume of the pyramid, three main vectors were used, edges vectors and the base surface represented by the figure below (Figure 3.8):

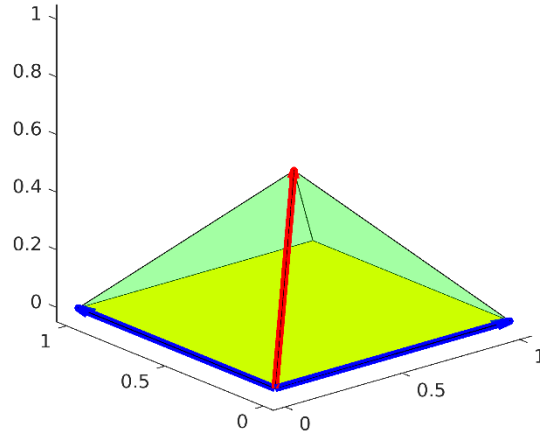


Figure 3.8 Vectorial distribution of the subelement

The volume of pyramidal is connected to the base surface and its height. The formula of the subelement volume is shown below:

$$\Delta V_{sub} = \frac{S_{Base} \dot{H}}{3} \quad (3.12)$$

$$H = \frac{V_1 \cdot V_2 \times V_3}{3 \|V_3 \times V_3\|} \quad (3.13)$$

Where V_1 is the eddy vector and V_2 and V_3 are the base vectors.

The last part is to calculate the surface area of the base. For that, the surface was divided into sub-surfaces based on the centre of gravity of the surface, and each sub-surface is computed to calculate the total surface as:

$$S_{base} = \sum \Delta S \quad (3.14)$$

$$\Delta S = \frac{\|V_{s1} \times V_{s2}\|}{2} \quad (3.15)$$

Where V_{s1} and V_{s2} are the vectors shown in Figure 3.9.

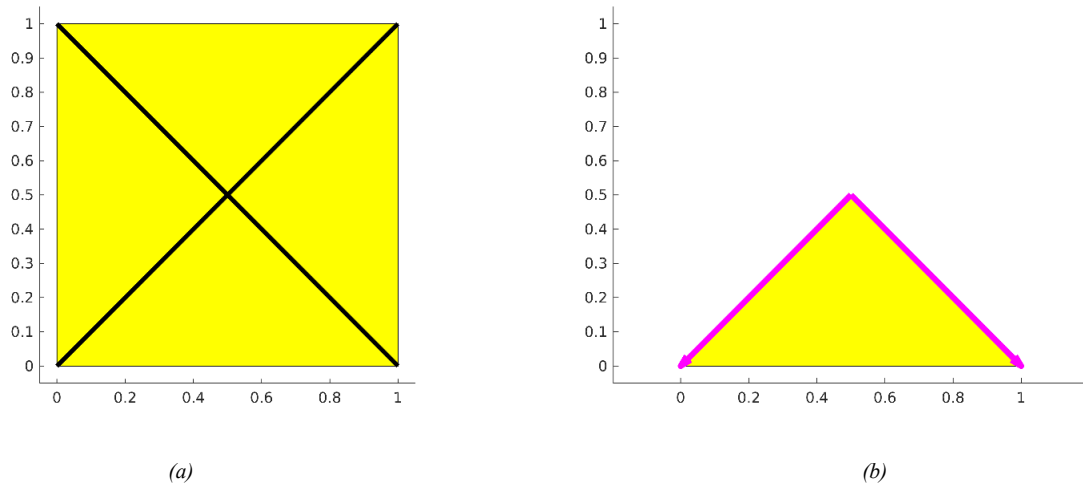


Figure 3.9 Base break down of the subelement. (a) Entire surface of the subelements with division. (b) Surface of lower subelement

After using this procedure, it was possible to calculate the volume of the recirculation zone on the Ahmed body. This result was computed in C++ and compared with the standard function for it in ParaView. Figure 3.10 and Table 3.5 below show the results of that extraction.

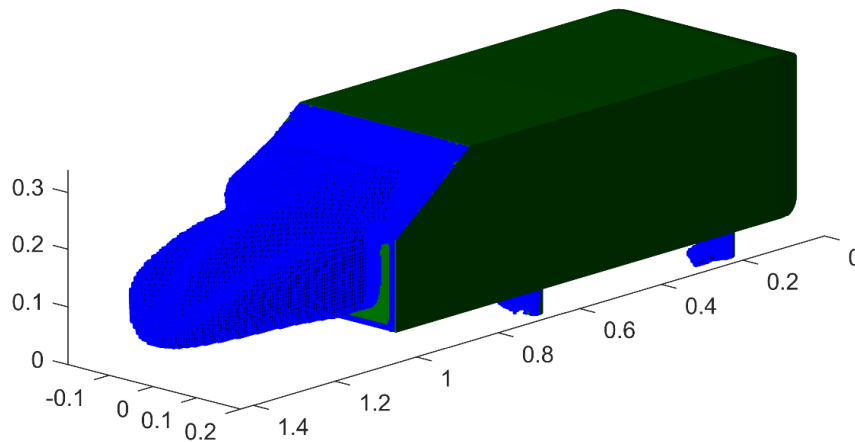


Figure 3.10 Recirculation zone captured

Table 3.5 Results of the recirculation zone quantification

	Present method	ParaView	Error (%)
Volume computed (dm ³)	15.5822	15.5832	0.0064

The results from the proposed method were compared with the calculator in ParaView. As mentioned before, the main source of error is if the faces of the element or the element itself are not convex. The volume of each element can only be calculated accurately if both are convex. Some elements due to bad meshing may not be entirely convex, resulting in a miss calculation of the volume. Nonetheless, the overall error is negligible, as shown in Table 3.5.

3.4 Geometry Generation Using B-spline

For this thesis, B-spline was used as a function to design the devices. However, the end goal does not need to be restricted to only B-splines approaches. B-splines curves of order k are generated by using a linear combination of polynomials of order $k-1$ and continuity C^{k-2} over the control points P [86]. The knot basis curves are generated based on breakpoints (knot vector $T = (t_0, t_1, \dots, t_m)$) using the following formula:

$$N_{i,1}(t) = \begin{cases} 1 & \text{for } t_i \leq t < t_{i+1} \\ 0 & \text{otherwise} \end{cases} \quad (3.16)$$

$$N_{i,k}(t) = \frac{t - t_i}{t_{i+k-1} - t_i} N_{i,k-1}(t) + \frac{t_{i+k} - t}{t_{i+k} - t_{i+1}} N_{i+1,k-1}(t) \quad (3.17)$$

With the formulas above, it is possible to generate the base curves that will compose the B-spline surfaces. To generate those base curves $N_{i,k}(t)$, a uniform knot vector (0,1) was used because it improved the accuracy and simplified the mesh for the mesh generation for the

STL(STereoLithography) files. According to Patrikalakis [86], repeating the breakpoints by k will force the curves to end at the last points, so the number of points of the knot vector will be $2k+n+1$ where k is the order of the B-spline and $n+1$ is the number of control points. That way is possible to control the beginning and the end of the surface.

Lastly, by using the base curves $N_{i,k}(t)$, it is possible to generate the B-spline surfaces by making the linear combination between the base curves (Equation (3.17)) and the control points using the formula below (Equation (3.18)). The genetic algorithm was applied to the position of the control points. Using different sets of control points, it is possible to generate many kinds of curves of order 3. Figure 3.11 and Figure 3.12 show the surfaces generated with a set of control points (cross points) and how they become attached to the Ahmed body.

$$\mathbf{r}(u, v) = \sum_{i=0}^m \sum_{j=0}^n \mathbf{p}_{ij} N_{i,k}(u) N_{j,l}(v) \quad (3.18)$$

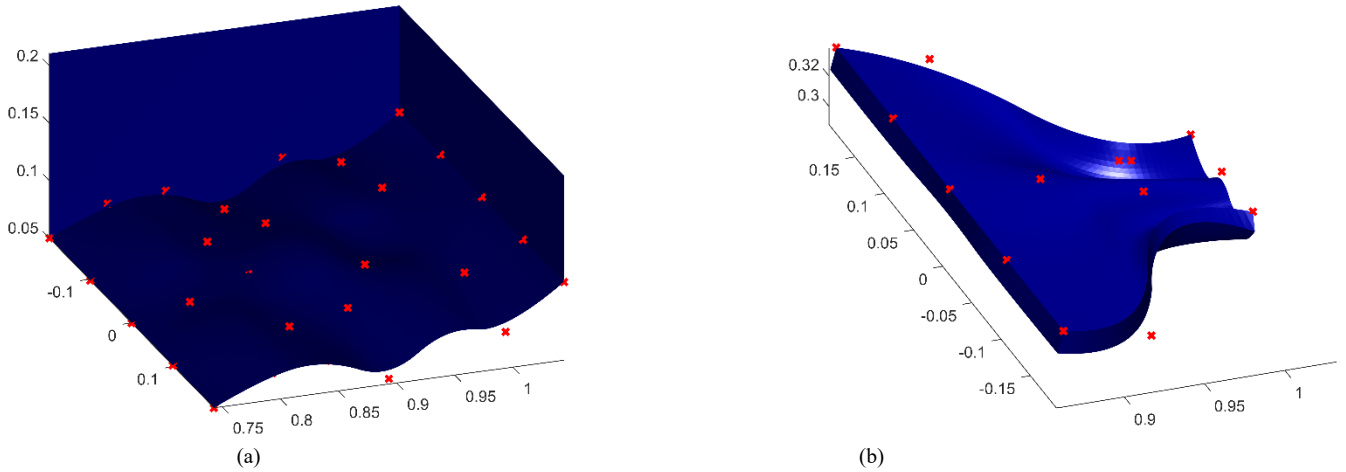


Figure 3.11 Surface generations. (a) Diffuser surface and (b) flap surface

Combining these surfaces shown in Figure 3.11, it is possible to generate the remaining parts of the devices and attach them to an Ahmed body as shown by Figure 3.12, which contains a whole Ahmed body with the surfaces presented before in Figure 3.11.

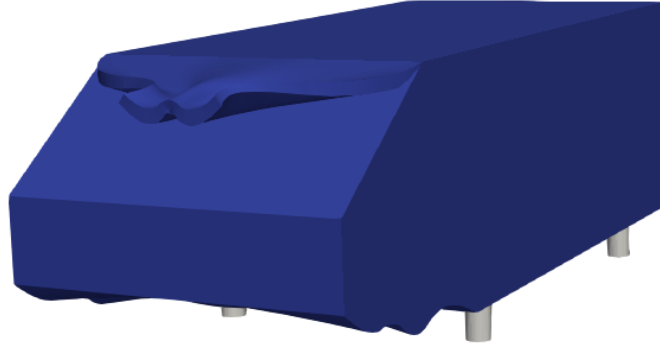


Figure 3.12 Full Ahmed body with a flap and a diffuser

Lastly, it was used as a gradient technique to close the flap geometry to extrude the flap. The gradient in each point was calculated to make the extrusion, and the down part of the flap is generated by the following formula:

$$(x_{i_2}, y_{j_2}, F_{ij_2}) = (x_i, y_j, F_{ij}) + G_{ij} \cdot t / \|G_{ij}\| \quad (3.19)$$

Where G is the gradient of the function $F(x,y)$, and t is the thickness of the.

Now, the formula of the gradient is simple, and it was calculated using first-order finite-difference, as shown in the formula below.

$$G_{ij} = (F_{ij_x}, F_{ij_y}, -1) \quad (3.20)$$

$$F_{ij_x} = \frac{F_{ij} - F_{i-1,j}}{x_i - x_{i-1}} \quad (3.21)$$

With Equation (3.20) and Equation (3.21), it is possible to calculate the gradient of $F(x,y)$ in every single point and finish the flap without any issues. It was used as a first-order scheme for simplicity, but for further improvement, higher-order schemes can be used.

3.5 Integration of NSGA-II, B-spline and OpenFOAM

The flowchart below describes how the NSGA-II, B-spline and OpenFOAM are integrated. The figure is divided into two parts, the first one (Figure 3.13(a)) shows how the entire algorithm works, while Figure 3.13(b) shows only how the evaluation of each individual population happens. The whole algorithm (Figure 3.13(a)) starts generating a random population size. After that, an evaluation will happen to import the objective functions. In this case, it will be the drag, lift and recirculation size. After all the evaluation happens, a genetic operator actions will start (crossover and mutation) to generate a new population. When this new population is generated, they will be evaluated, and then a selection will happen again. This will continue until the user decides to stop. Note that the evaluation of each individual population how the integration between NSGA-II, B-spline and OpenFOAM happens (Figure 3.13(b)). When the population is generated, each individual member of the population will have a chromosome that will be translated into a B-spline surface that is going to be written in the STL format and exported to the CFD. After this exporting happens, a meshing and turbulence model will take place, and it will follow the procedures explained in the previous sections to collect results.

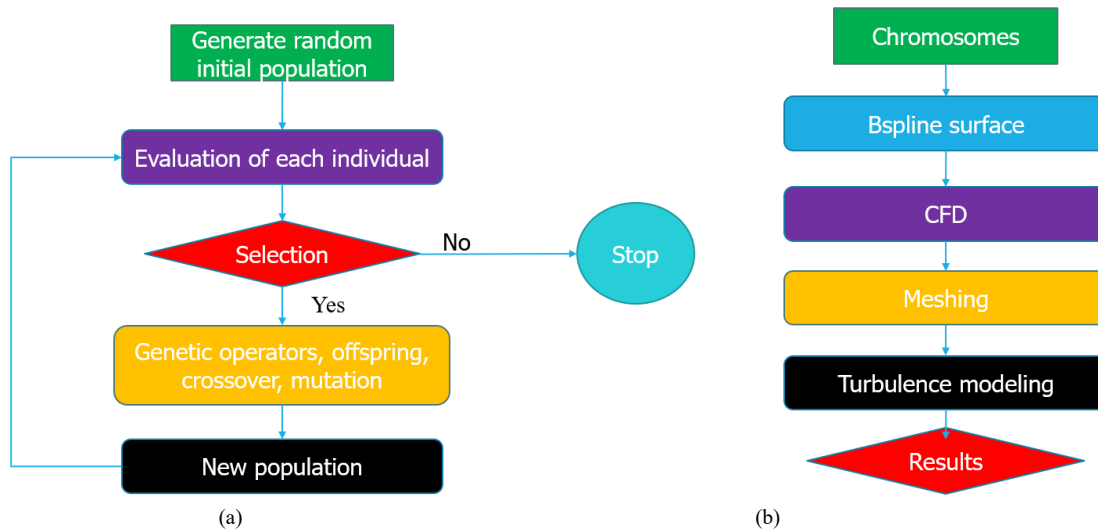


Figure 3.13 Flowchart of the B-spline, NSGA-II and OpenFOAM integration. (a) Whole algorithm flow chart and (b) evaluation of each individual member of the population flow chart

Chapter 4 Results and Discussion

This chapter is dedicated to the results and discussion. All the results will be presented and discussed based on the physics of fluid dynamics. It is necessary to discuss the physical meaning behind the results to provide some insight. The chapter is divided into five main sections.

4.1 Implementation of the Proposed Method

The method was applied to optimize flap or diffuser or both for aerodynamic drag and lift reduction or soiling reduction. In all the scenarios considered in this study, the method implemented to run for the same time span, starting with random genes. This way, the number of generations achieved depended on the computational cost of individual members of the population run. In the end, it was observed that the method was able to reach 15-18 generations with a population size of 20 for all cases, except for the soiling, which was 10. The soiling optimization had half of the time span, and because of that, the population size was reduced.

Figure 4.1 shows the progression of the solution from one generation to another. The closer the points approach the intersection of the vertical and horizontal axes, the better. From Figure 4.1, it can be observed that there are significant differences between the individual members of the population in the 1st generation and those of the 15th -18th generations, showing the evolution from generation to generation. For better results, the method should be allowed to run for several generations. However, due to limited computational resources, it could only achieve 15 -18 generations. Nonetheless, the number of generations is sufficient to evaluate the performance of the method developed in this thesis. It should be noted that for a single run of the method, several unique geometries can be generated, up to 70 geometries. More importantly, each of the geometries is optimized based on the specified objectives, in this case, drag reduction or lift reduction or

soiling reduction or a combination. Sample geometries will be displayed in the following sections.

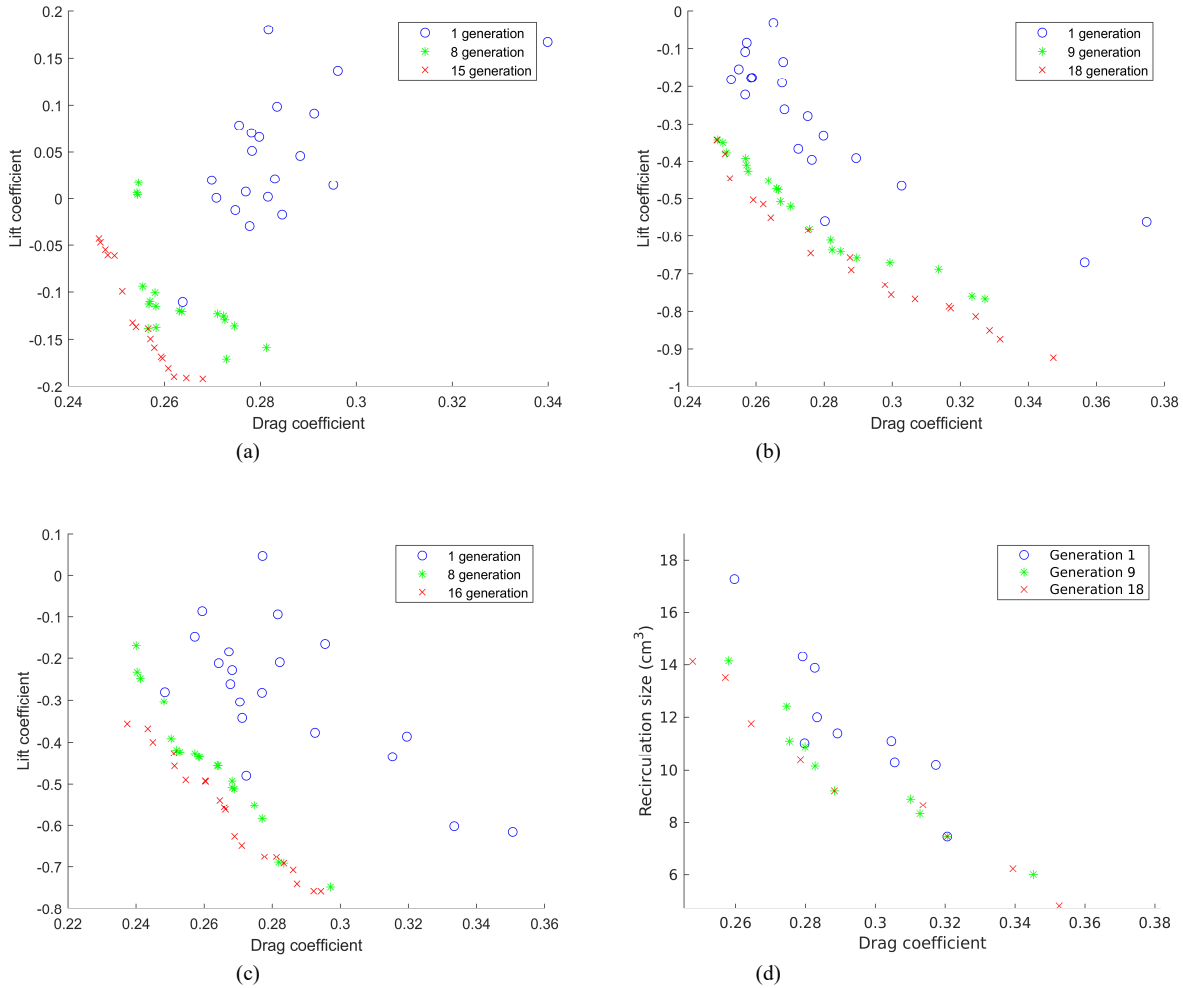


Figure 4.1 Progression of the solutions with generations for the optimization of (a) flap for drag and lift (b) diffuser for drag and lift (c) combined flap and diffuser for drag and lift (d) flap for drag and soiling

4.2 Flap Optimization for Drag and Lift

Figure 4.2 displays sample unique flap geometries generated by the proposed method. From these, Figure 4.2(d) was selected for further analysis. A detailed CFD analysis was performed on it to obtain the aerodynamic forces shown in Table 4.1.

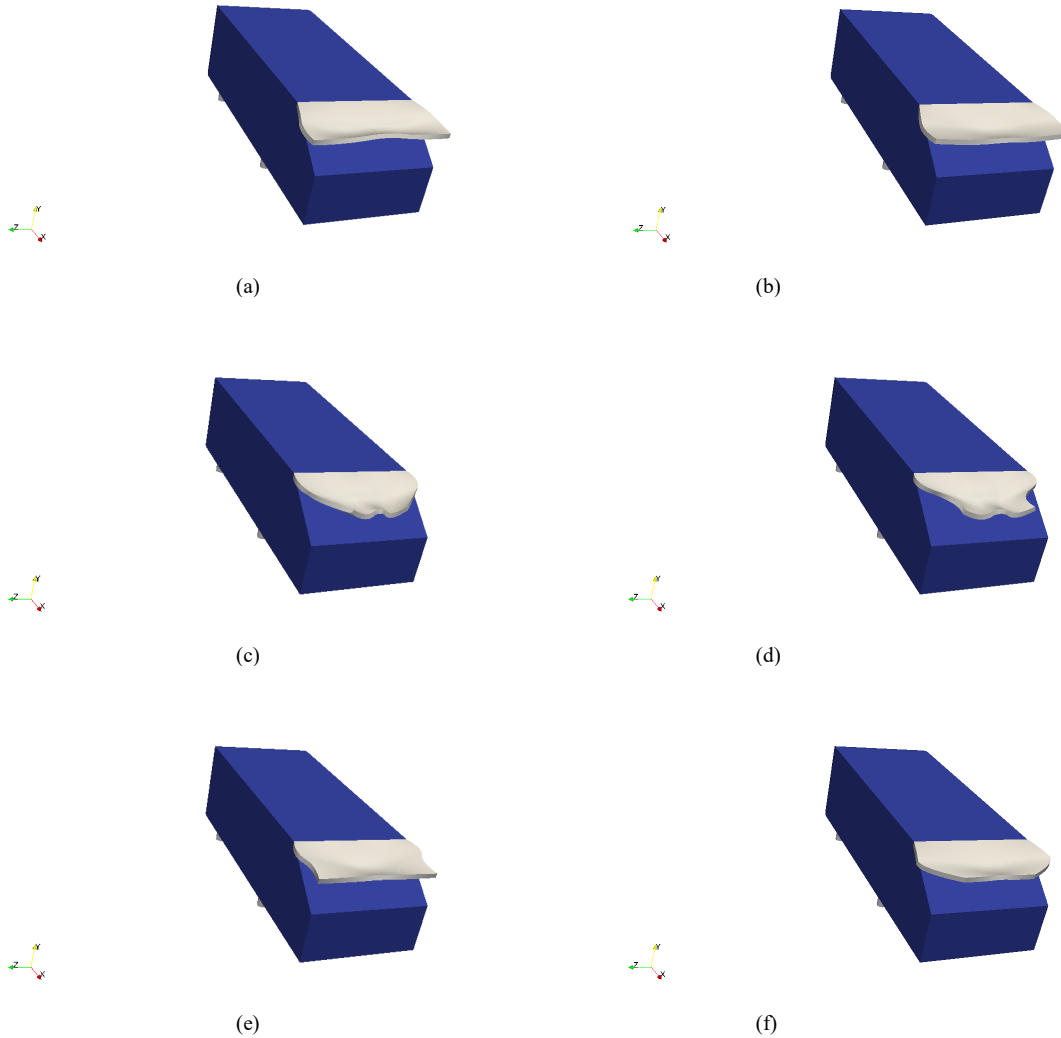


Figure 4.2 Samples of the result of the flap optimization for drag and lift

Table 4.1 Drag and lift coefficients for the selected flap geometry in Figure 4.2(d)

Coefficient	Absolute value	Improvement
Drag, C_d	0.2464	7.7%
Lift, C_l	-0.0430	379.2%

Table 4.1 shows that the selected flap produced a drag reduction of 7.7% compared with the base model and lift reduction (increase in downforce) of 379.2%. Therefore the flap is more favourable to generating downforce than drag reduction. There are two main contributing factors for an increase in drag on a vehicle, including the recirculation zone and also longitudinal vortices

[87]. It is also important to mention that, according to Delassaux, longitudinal vortices are responsible for not only generating drag but also lift [88]. In addition, according to Aider, drag is related to the separation bubble and the longitudinal vortices [87]. Therefore, reducing the effect of one or the other will cause a drag reduction.

Figure 4.3 shows that the pressure at the rear is increased relative to the base model, which resulted in a reduction in drag, as already shown in Table 4.1. The low-pressure contours are attached to the Ahmed body in Figure 4.3(a), but in Figure 4.3(b), it is far from the body, justifying the drag reduction. In addition, there is a sudden increase in pressure on top of the flap, also increasing downforce. These observations will be further explained in terms of flow features.

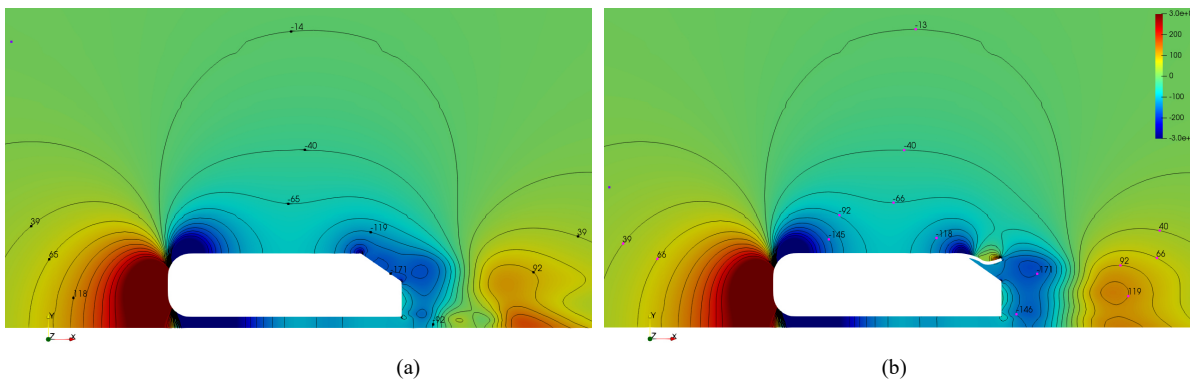


Figure 4.3 Pressure contours for (a) baseline and (b) optimized flap

Figure 4.4 shows that the contours of the velocity magnitudes ($U_{\text{mag}} = \sqrt{u^2 + v^2 + w^2}$, where u, v, w are the velocity components in x, y, z directions respectively). It can be observed that the recirculation is slightly reduced relative to the base model. Figure 4.4(b) shows that the flow separated and reattached to the flap. As mentioned earlier, keeping the flow attached to the surface is one of the drag reduction mechanisms. Another observation in Figure 4.4 is that the concave shape of the flap slowed down the flow on top of it and thus increasing pressure. This behaviour is consistent with the pressure contours in Figure 4.3(b). As mentioned earlier, there is an increase in pressure at the end of the flap.

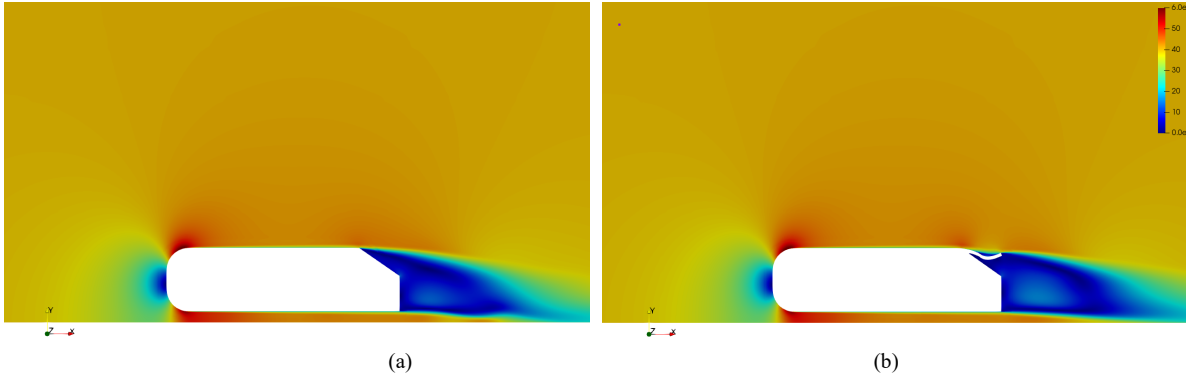


Figure 4.4 Velocity magnitude for (a) baseline and (b) optimized flap

In addition, Figure 4.5 shows the contour plots of vorticity $\{\vec{\omega} = (\frac{\partial w}{\partial y} - \frac{\partial v}{\partial z}, \frac{\partial u}{\partial z} - \frac{\partial w}{\partial x}, \frac{\partial v}{\partial x} - \frac{\partial u}{\partial y})\}$. It shows that the instantaneous vorticity is slightly reduced in the optimized flap compared to the base case. In Figure 4.5(a), the vorticity is thicker than in Figure 4.5(b), vortices demonstrating that the longitudinal vortices are weaker. This is consistent with the observation made by Aider, who used the same procedure to compare the longitudinal vortices [87].

Figure 4.6 shows the helicity contours. By definition, helicity is $H = \vec{U} \cdot \vec{\omega}$, where $\vec{\omega}$ is the vorticity vector and \vec{U} velocity vector. Viswanathan [89] compared C-pillar vortices (longitudinal vortices) using this method. Figure 4.6 shows a reduction in C-pillar vortices as the vortices are shorter in (b) than in (a), where the contours extend to the end of the wake. This is further evidence that the vortices in Figure 4.6(a) have more energy and are stronger than in Figure 4.6(b).

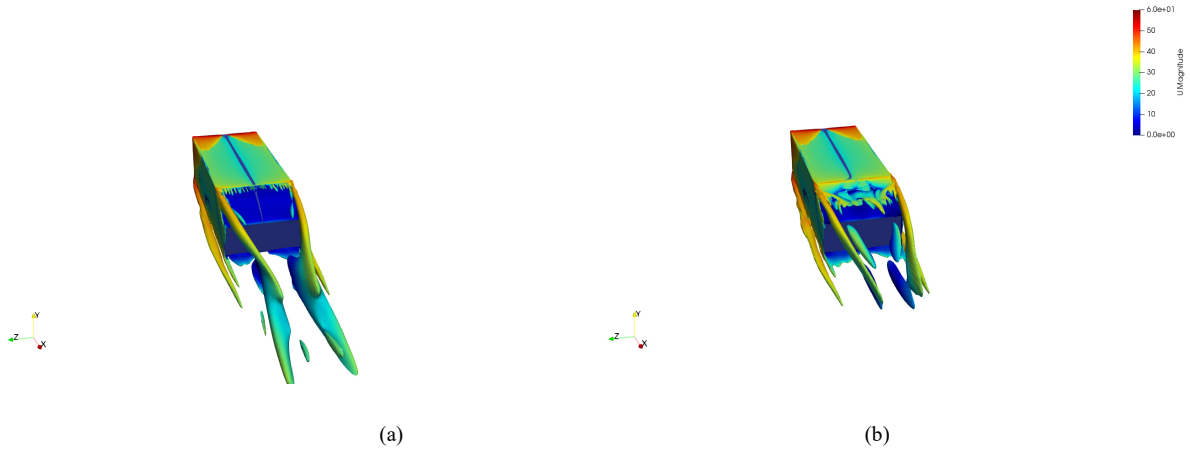


Figure 4.5 Contour plots for vorticity $\omega_x = 200/s$ on x -component for (a) baseline and (b) optimized flap

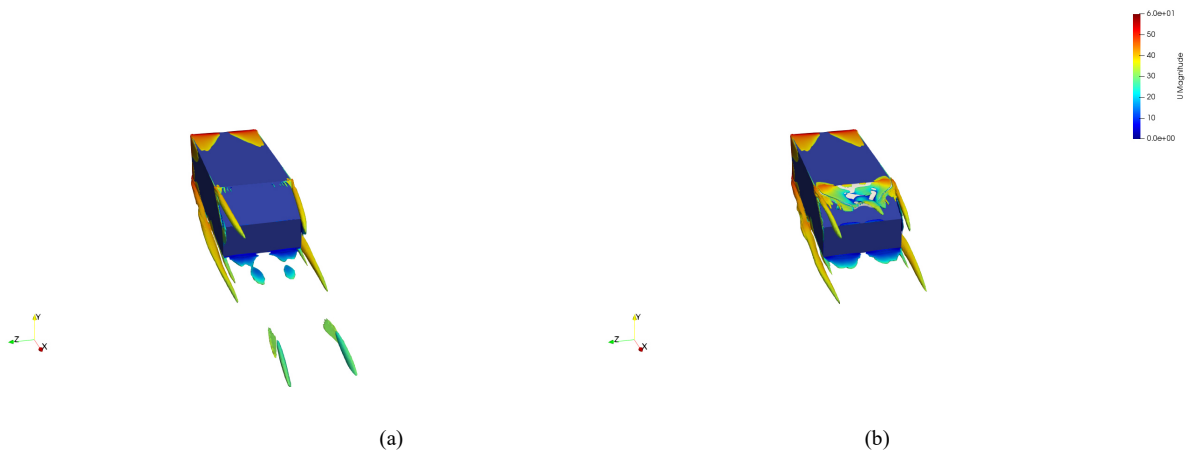


Figure 4.6 Contour plots for helicity $H = 7500m/s^2$ for (a) baseline and (b) optimized flap

Figure 4.7 illustrates the comparison between Q -criterion, as defined in Equation (2.4). It can be observed that the longitudinal vortex for Figure 4.7(a) is extended into the wake region, whereas Figure 4.7(b) is dissipated immediately, indicating weaker longitudinal vortices. In Figure 4.7, it is not very clear the reduction in the vortices because they are not strong enough.

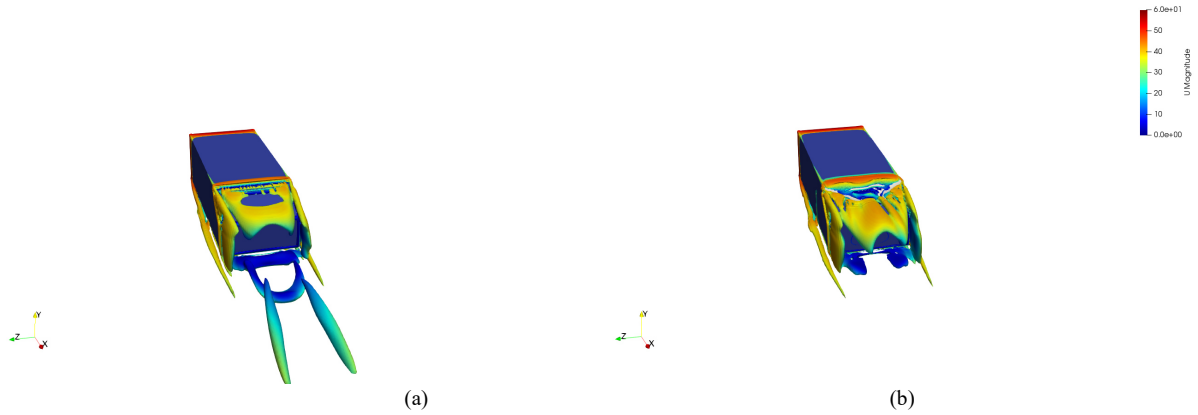


Figure 4.7 Contour plots for Q -criterion, where $Q/U_{ref} = 150$ for (a) baseline and (b) optimized flap, where U_{ref} is the inlet velocity

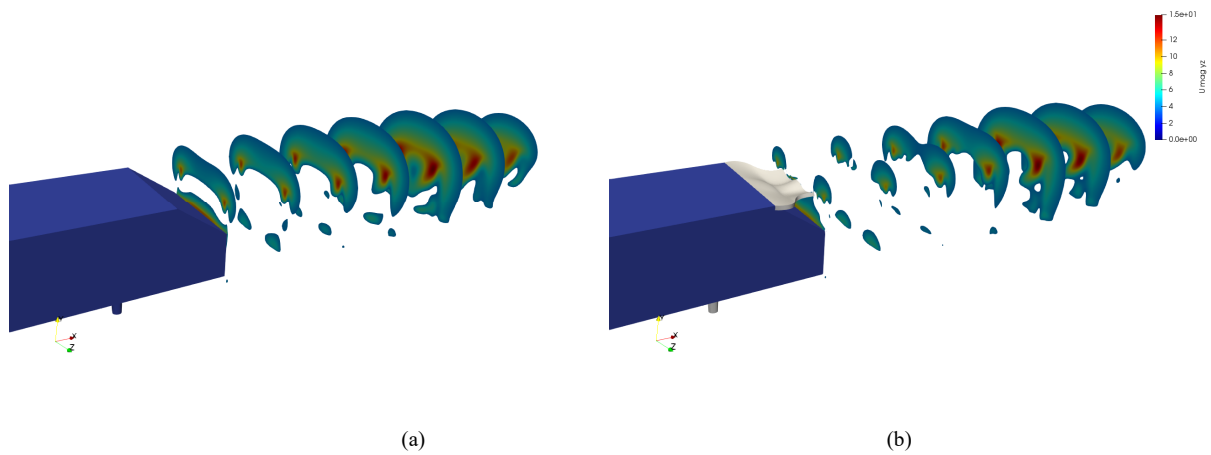


Figure 4.8 Contour plots for velocity magnitude for the y - and z -components for (a) baseline and (b) optimized flap

Lastly, Figure 4.8 illustrates clearly the small sizes of the contours in Figure 4.8(b). Figure 4.8(b) shows that the vortices start much weaker and then regain some strength downstream in the wake region. This behaviour will increase the pressure near the Ahmed body and shifts the lower pressure region away from the body, resulting in both drag and lift reduction, as shown in Figure 4.3. These longitudinal vortices are responsible for increasing drag and lift [88], if formed on the upper region.

4.3 Diffuser Optimization for Drag and Lift

Figure 4.9 displays sample unique diffuser geometries generated by the method developed

in chapter 3. Figure 4.9(a) was selected for further analysis from these geometries. From a more detailed CFD analysis, the aerodynamic forces of this geometry are shown in Table 4.2.

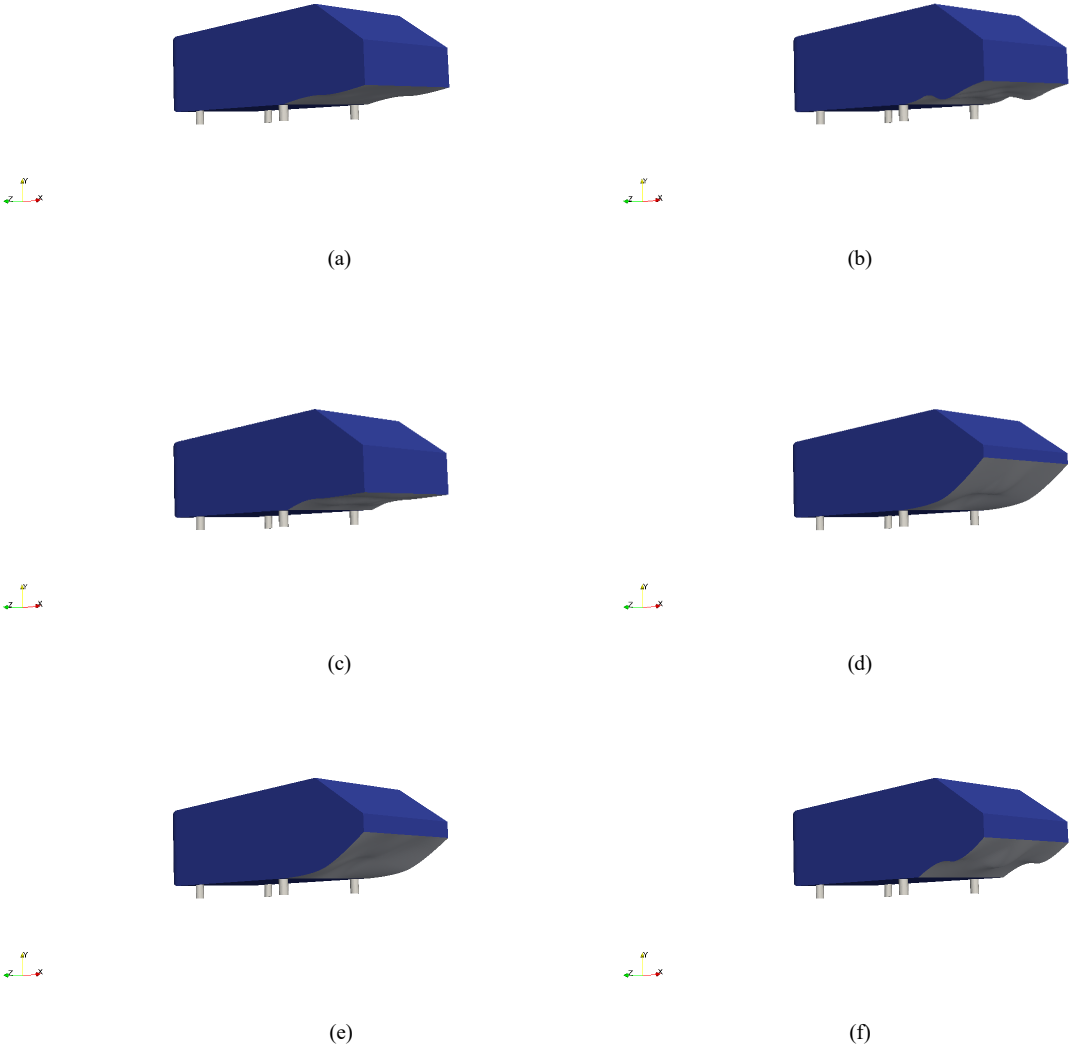


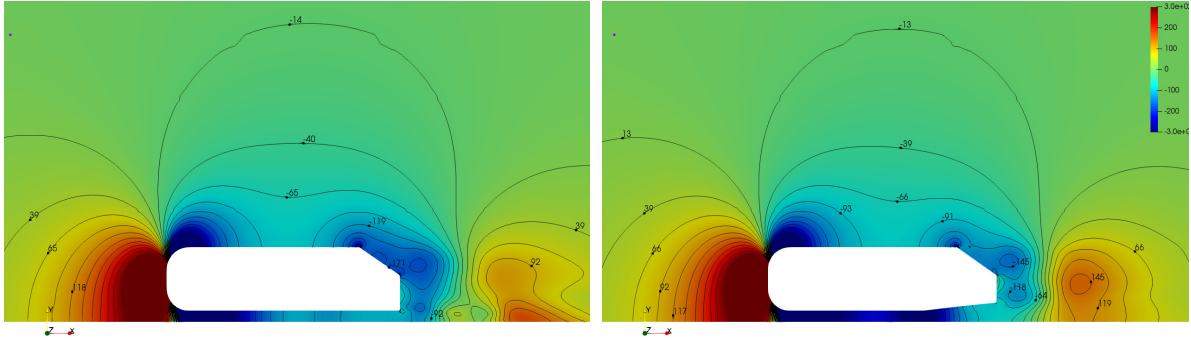
Figure 4.9 Samples of the result of the diffuser optimization for drag and lift

Table 4.2 Drag and lift coefficients for the selected diffuser geometry in Figure 4.9(a)

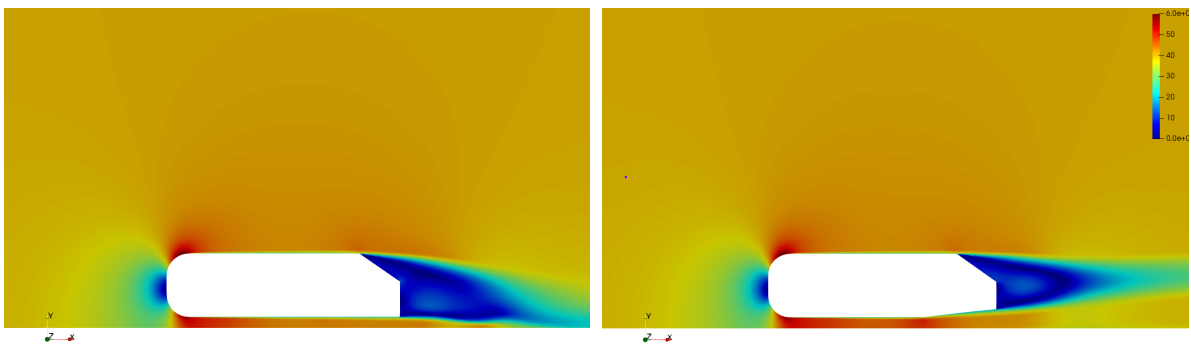
Coefficient	Absolute value	Improvement
Drag, C_d	0.2486	6.9%
Lift, C_l	-0.3961	2672.1%

This diffuser is the one that produces the least drag among all the geometries shown in Figure 4.9. This model produced a drag reduction of 6.9% relative to the base model and 2672.1% for lift reduction (or increase in downforce). Similar to the previous cases, two main factors affect the results, the recirculation zone and longitudinal vortices. Keeping the flow attached to the diffuser reduces drag, as mentioned by Moghimi [90]. In his research, he deduced that the angle of the diffuser has an effect on drag and on the efficiency of lift reduction. His results showed that the diffuser that produces the least drag was the diffuser with the highest angle without flow separation. Although longitudinal vortices usually increase drag underneath the Ahmed body, they also increase the downforce. George [91] and Zhang [92] mentioned in their studies that there is higher downforce in the diffuser with greater longitudinal vortices.

Figure 4.10 shows the pressure contours and indicates a significant decrease in pressure under the Ahmed body near the neck of the diffuser relative to the base model. This resulted in an increase in downforce, as shown in Table 4.2. Furthermore, there is also an increase in pressure on the upper rear part of the Ahmed body in Figure 4.10(b) relative to the base model, Figure 4.10(a). This is also reflected in a reduction in drag. The velocity magnitudes in Figure 4.11(b) shows the flow keeps fully attached to the Ahmed body. This behaviour is consistent with the findings of Moghimi [90]. As mentioned earlier, his results showed that the diffuser with the least drag was the one with the highest opening with no flow separation. In fact, the diffuser generated by the algorithm is quite similar to the one reported by Moghimi [90]. This illustrates that the proposed method is effective. In addition, it can be observed that the flow is accelerated under the Ahmed body Figure 4.11(b), causing low pressure under the body, as shown in Figure 4.10(b).



(a) (b)
 Figure 4.10 Pressure contours for (a) baseline and (b) optimized diffuser



(a) (b)
 Figure 4.11 Velocity magnitude for (a) baseline and (b) optimized diffuser

Figure 4.12 and Figure 4.13 show that the longitudinal vortices on the upper part are significantly reduced for the optimized diffuser relative to the base model. This reduction reflects the behaviour mentioned in Figure 4.10(b) about the increase in pressure on the upper part of the rear. Although the longitudinal vortices are reduced on the upper part, they increase underneath the Ahmed body. However, as mentioned earlier, this will increase the downforce. Although these lower vortices are responsible for increasing the drag, the flow for this case is fully attached to the diffuser resulting in the drag reduction.

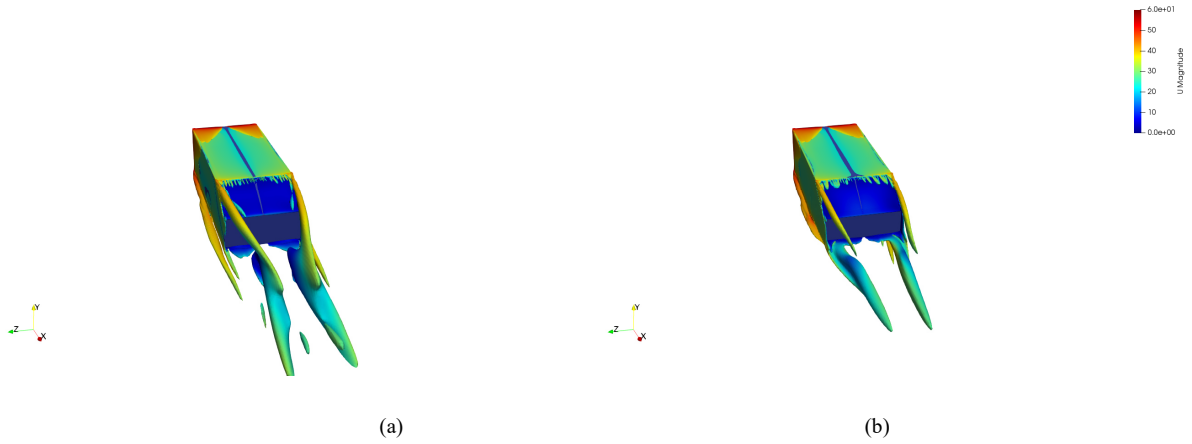


Figure 4.12 Contour plots for vorticity $\omega_x = 200/s$ on x -component for (a) baseline and (b) optimized diffuser

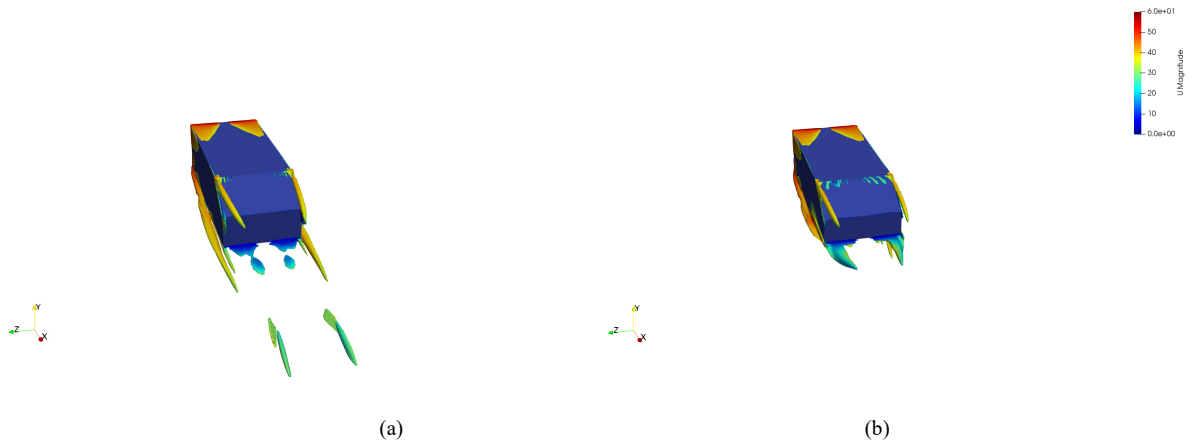


Figure 4.13 Contour plots for helicity $H = 7500m/s^2$ for (a) baseline and (b) optimized diffuser

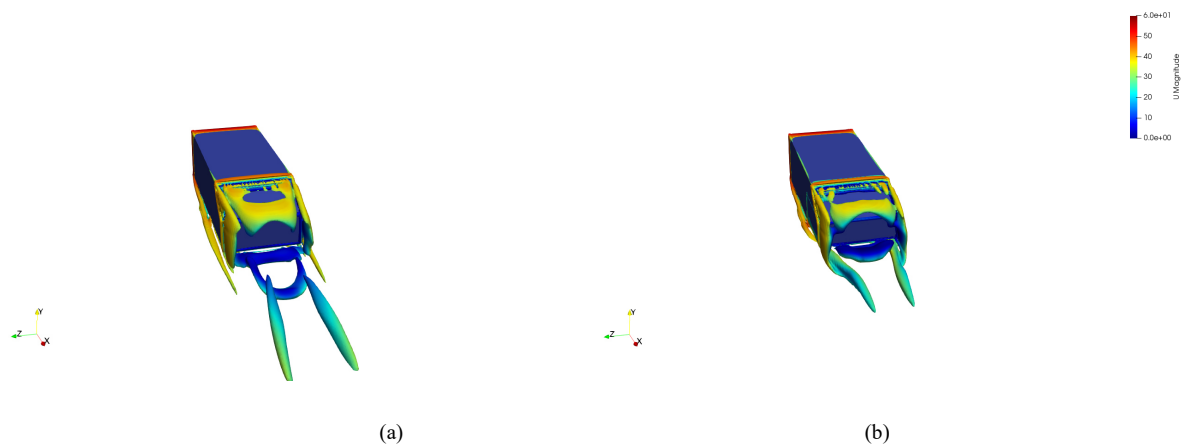


Figure 4.14 Contour plots for Q -criterion, where $Q/U_{ref} = 150$ for (a) baseline and (b) optimized diffuser

Figure 4.14 shows the contours of the Q -criterion. It can be observed in Figure 4.14(b) that there is a formation of large vortices underneath the Ahmed body and smaller vortices on the upper part. This is evidence that the presence of the diffuser is weakening the vortices on the upper part. The upper vortices in Figure 4.14(a) extend further downstream into the wake, whereas they are dissipated more quickly in Figure 4.14(b). As mentioned earlier, there is drag reduction due to the flow being fully attached to the diffuser, allowing pressure recovery.

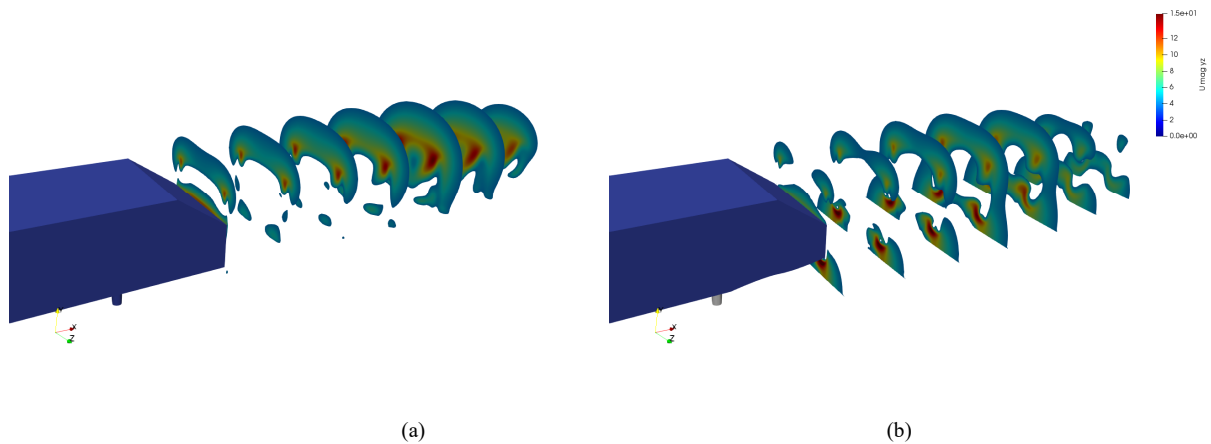


Figure 4.15 Contour plots for velocity magnitude considering y - and z - components for (a) baseline and (b) optimized diffuser

Lastly, Figure 4.15 shows contours of velocity magnitudes. There is a formation of longitudinal vortices under the Ahmed body (increase downforce) and a significant reduction of the longitudinal vortices on the upper region of the Ahmed body. As stated earlier, this results in a reduction of both drag and lift. All the results for this section are consistent with previous results [90].

4.4 Combined Flap and Diffuser Optimization for Drag and Lift

Figure 4.16(a) was selected for further analysis from these geometries because of its interesting geometry. From a more detailed CFD analysis, the aerodynamic forces of this geometry

(Figure 4.16(a)) were obtained, as shown in Table 4.3.

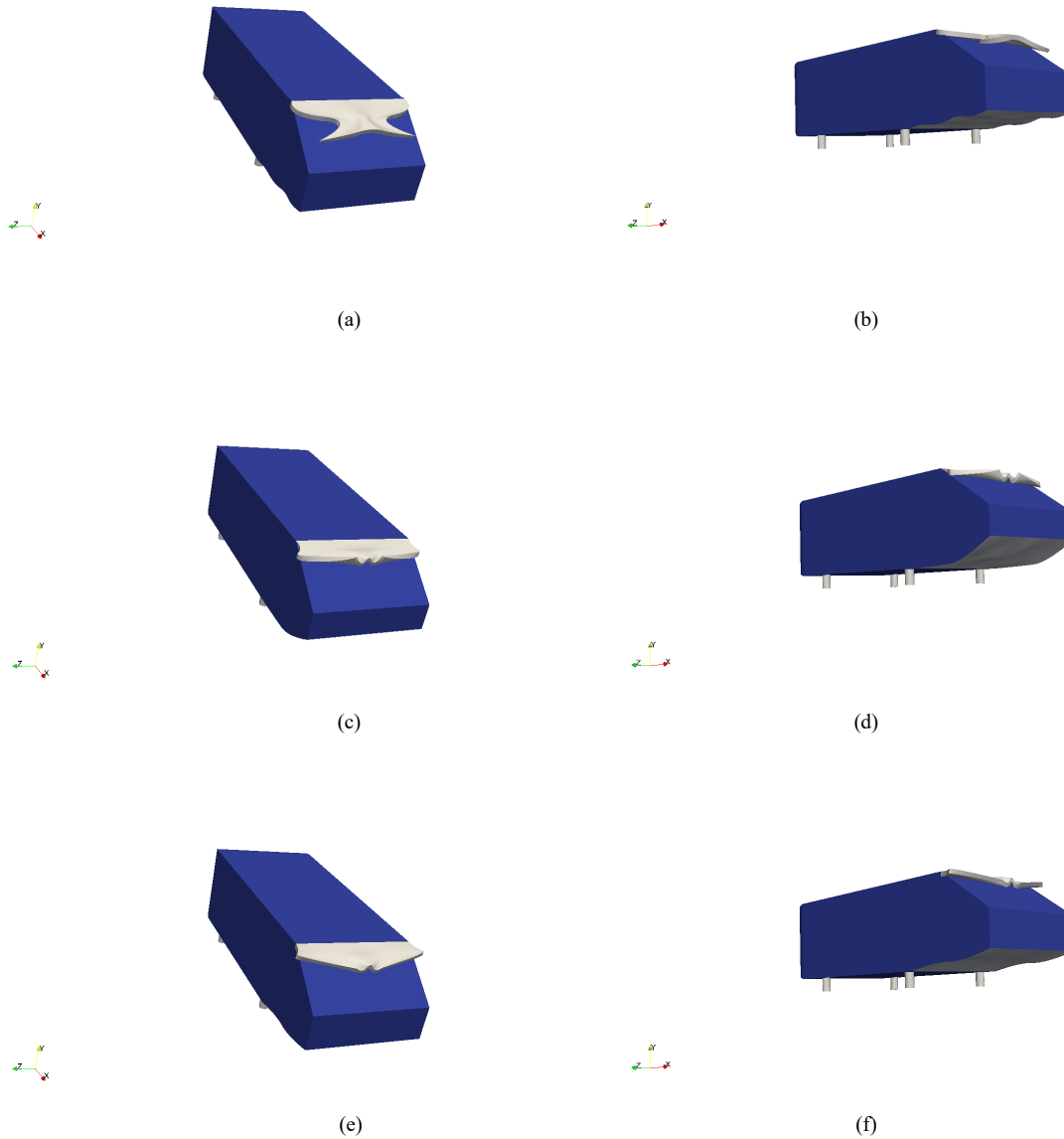


Figure 4.16 Samples of the result of the flap and diffuser optimization considering drag and lift where (a), (c) and (e) are the upper view and (b), (d) and (f) are the lower view of each sample

Table 4.3 Drag and lift coefficients for the selected flap geometry in Figure 4.16(a)

Coefficient	Absolute value	Improvement
Drag, C_d	0.2435	8.8%
Lift, C_l	-0.3686	2420.5%

This model produced a drag reduction of 8.8% relative to the base model and 2420.5% in

lift reduction (increase in downforce). The pressure contours in Figure 4.17 show that the base pressure is significantly increased by the flap and diffuser combination resulting in the drag reduction. Additionally, the convex shape of the diffuser significantly reduced the pressure at the underbody, which results in a downforce increase. A similar shape for the diffuser was also reported by Ehirim [33], but he only achieved a downforce increase of 4.8%. The combination of flap and diffuser contributed to the massive increase in downforce in this study. Interestingly the flap/diffuser combination has resulted in different geometries of the flap and diffuser compared to the geometries generated for the flap alone and diffuser alone that were discussed in the previous sections. Furthermore, Figure 4.18(b) shows a significant reduction in the recirculation region relative to the base geometry, which is consistent with the pressure results in Figure 4.17, Figure 4.19 and Figure 4.20 confirmed that the longitudinal vortices in the wake are significantly modified. The vortices at the upper region of the wake are much more reduced than in the lower region. The increase of those vortices on the lower region of the Ahmed body is evident in what was previously mentioned; the diffuser is more efficient at improving the downforce than reducing drag.

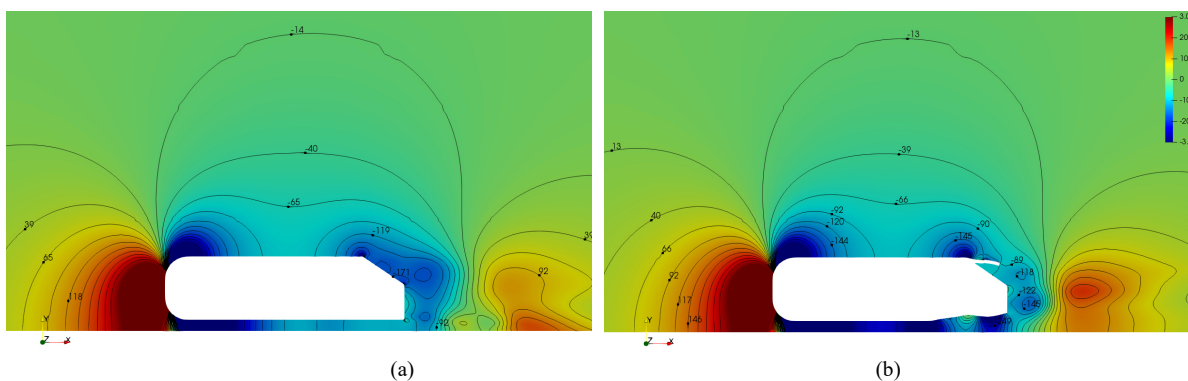


Figure 4.17 Pressure contours for (a) baseline and (b) optimized flap and diffuser

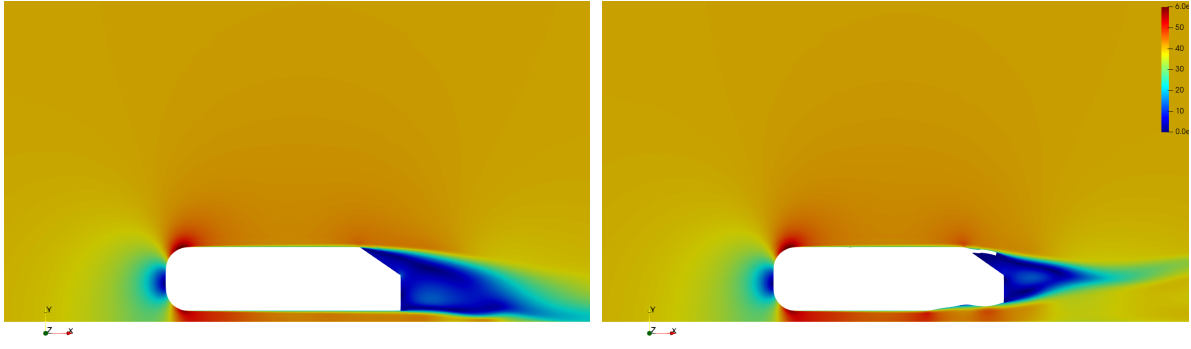


Figure 4.18 Velocity magnitude for (a) baseline and (b) optimized flap and diffuser

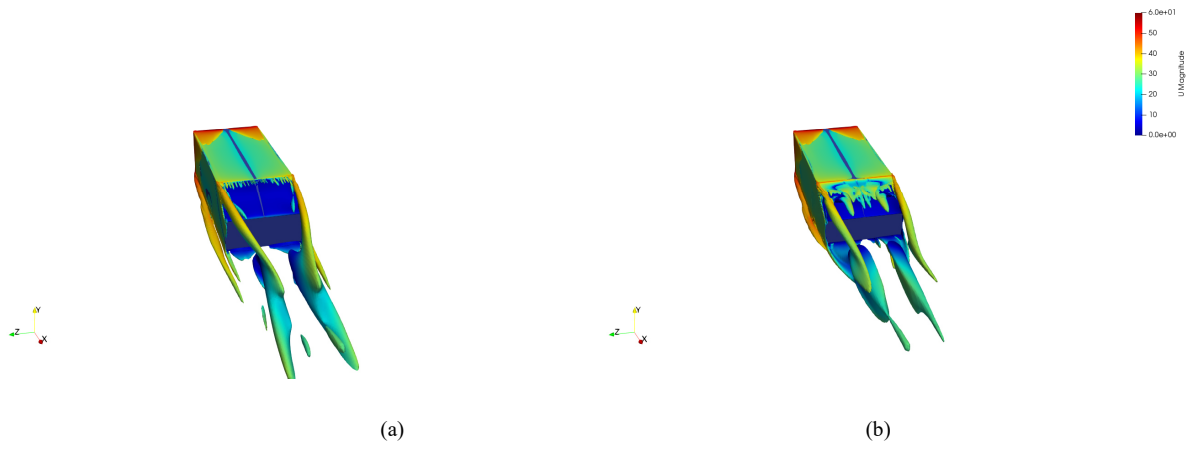


Figure 4.19 Contour plots for vorticity $\omega_x = 200/s$ on x -component for (a) baseline and (b) optimized flap and diffuser

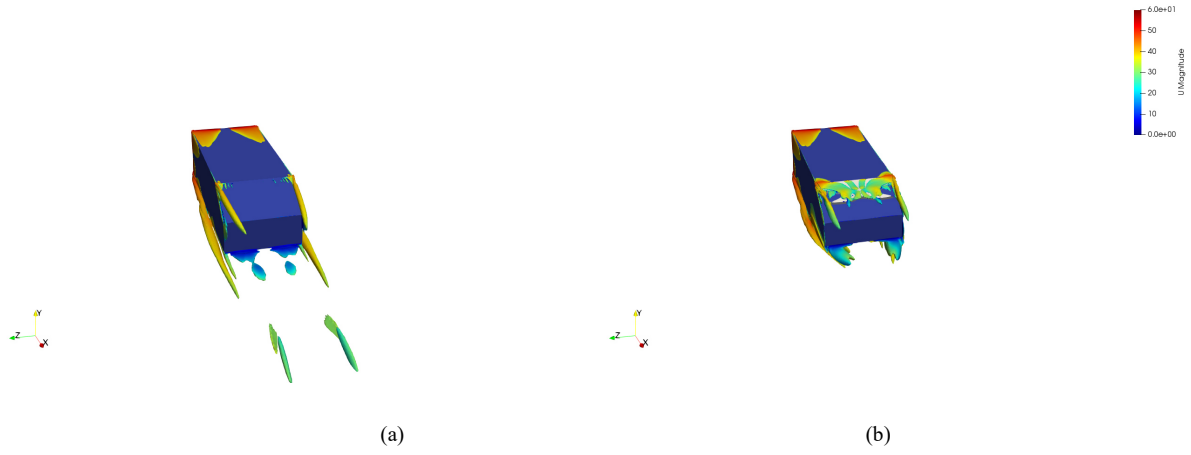


Figure 4.20 Contour plots for helicity $H = 7500m/s^2$ for (a) baseline and (b) optimized flap and diffuser

Figure 4.21 shows the contours of the Q -criterion as defined by Equation (2.4). It can be observed in Figure 4.21(b) that the vortices in the lower region of the wake are stronger than those

in the upper region, relative to the base model. Figure 4.22 also shows similar behaviour. These results are all consistent with those previously discussed.

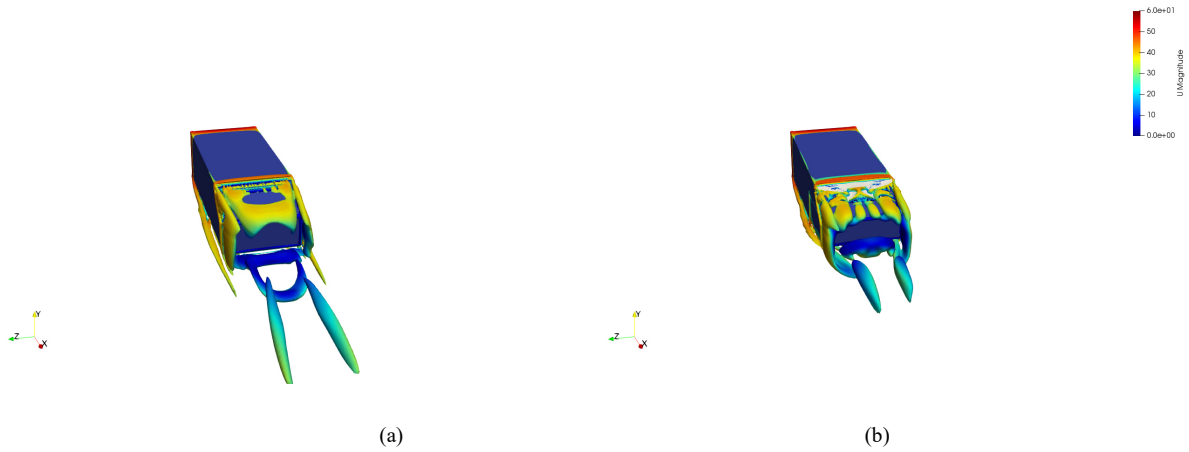


Figure 4.21 Contour plots for Q -criterion, where $Q/U_{ref} = 150$ for (a) baseline and (b) optimized flap and diffuser

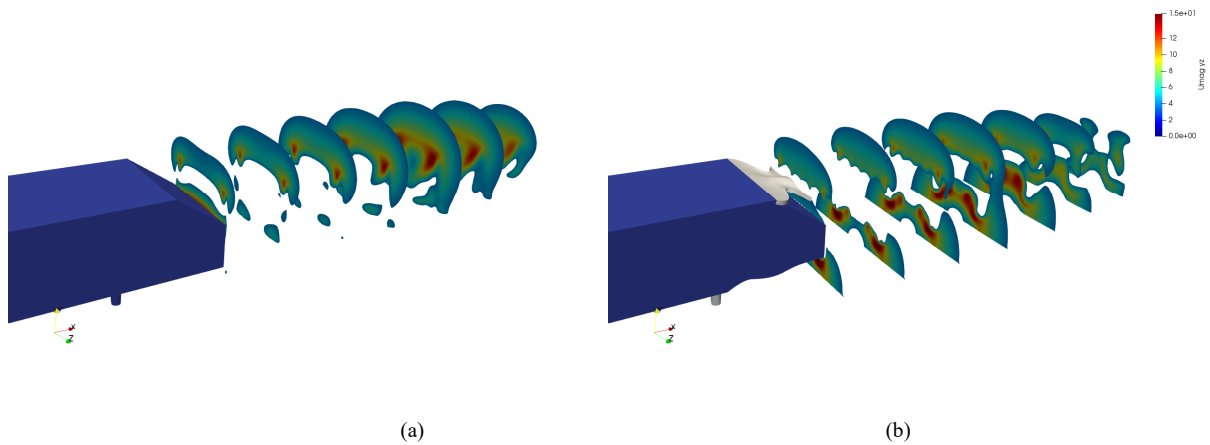


Figure 4.22 Velocity magnitude considering y - and z -components for (a) baseline and (b) optimized flap and diffuser

It is important to mention that the result found by combining the devices together in optimization is as promising as the optimization of the individual devices. The reason for that is the combination has a higher dimension (30 design variables) while the separate ones have 12 and 18. However, it is believed that the combined one can find better results if given more time to run. From the previous results (Figure 4.15), it can be observed that the diffuser affects the longitudinal vortices at the upper region. So it can be concluded that the diffuser can affect the upper wake. Because the upper region wake of the Ahmed body is affected by the diffuser, it is believed that

optimizing the flap and diffuser together can further enhance the drag and downforce features. However, it is more computationally expensive and could not be achieved due to a lack of time to run.

4.5 Flap Optimization for Drag and Soiling

From the unique geometries generated by the method and displayed in Figure 4.23, Figure 4.23(a) was selected for a more detailed CFD analysis, and the aerodynamic forces are shown in Table 4.4

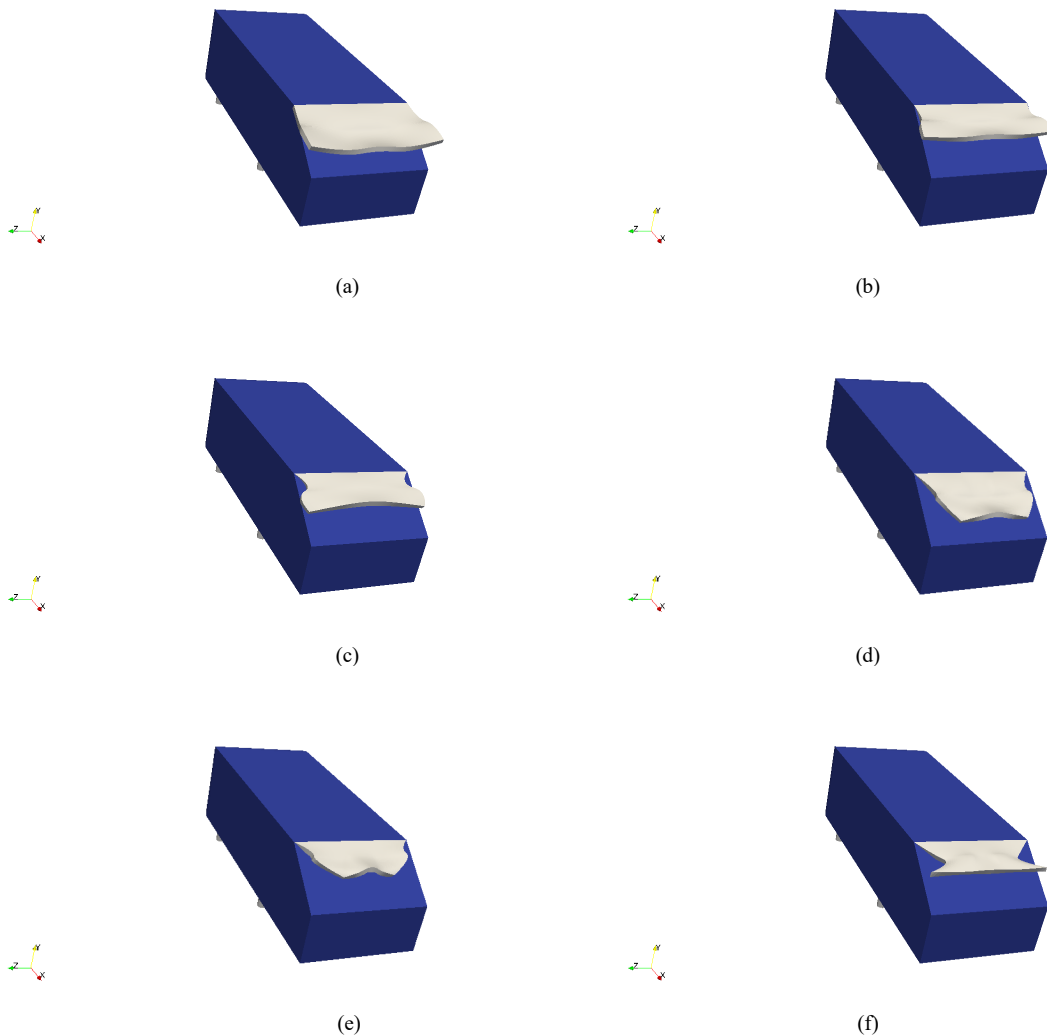


Figure 4.23 Samples of the result of the flap optimization considering drag and recirculation volume

Table 4.4 Drag coefficient and recirculation volume for the selected flap geometry in Figure 4.23(a)

Parameter	Absolute value	Improvement
Drag, C_d	0.2393	10.4%
Recirculation (cm^3)	14.3300	8.0%

This optimized geometry produced a drag reduction of 10.4% relative to the base model and an 8% reduction in the recirculation volume. Similar to the previous cases, two main factors affect the results, the recirculation zone and longitudinal vortices. From Figure 4.24(b), it can be observed that the flap is allowing a faster pressure recovery at the rear (increasing pressure at the rear), and thus reducing the drag.

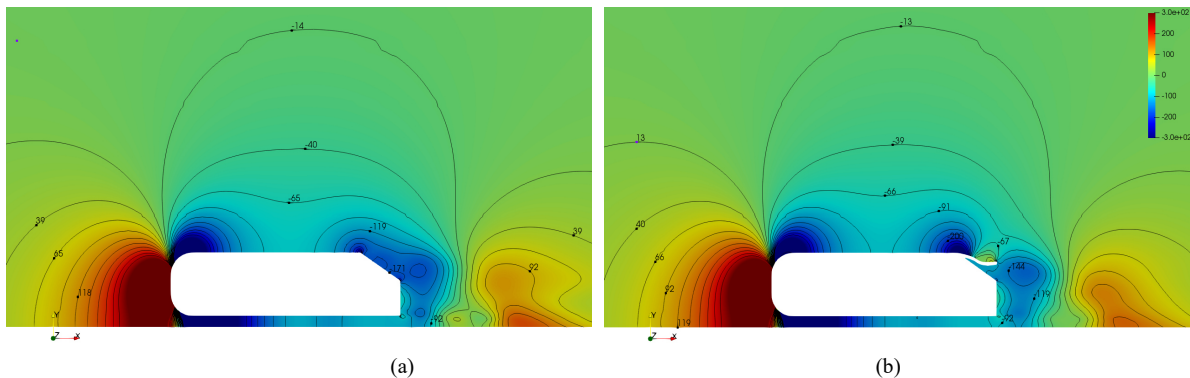


Figure 4.24 Pressure contours for (a) baseline and (b) optimized flap

From Figure 4.25(b), it is clear that when the algorithm reduced the size of the recirculation, the flow becomes more attached to the body. Although the recirculation zone is smaller for this scenario, the strength of longitudinal vortices was enhanced relative to the base model, as shown in Figure 4.26 and Figure 4.27. As mentioned earlier, the drag is affected by the recirculation zone and longitudinal vortices. It is the balance of these two that determine the drag. However, in the present scenario, the reduction in the recirculation outweighs the strength of the longitudinal vortices, resulting in a significant drag reduction.

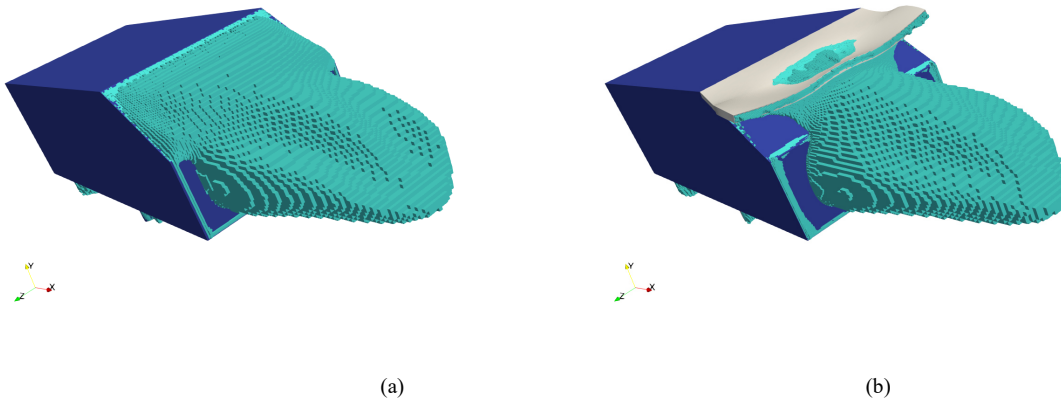


Figure 4.25 Recirculation zone for (a) baseline and (b) optimized flap

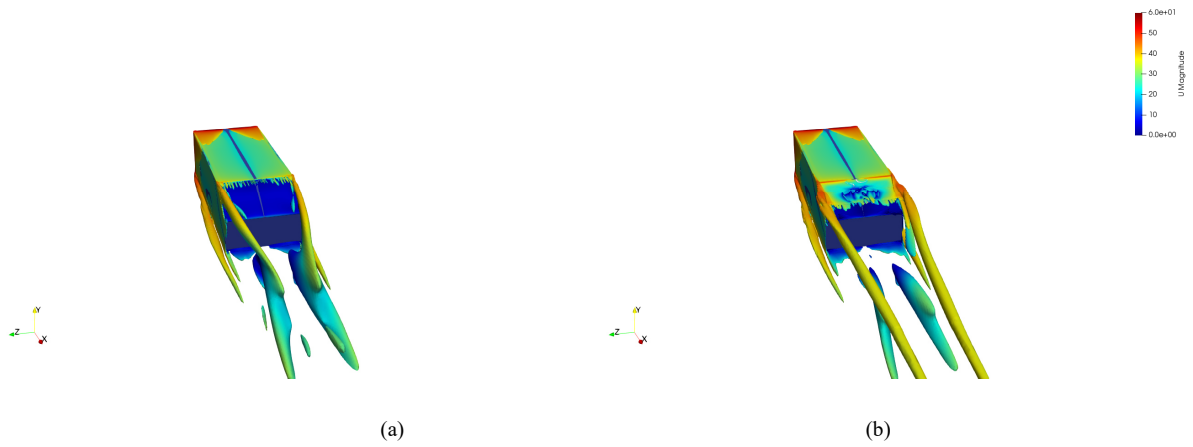


Figure 4.26 Contour plots for vorticity $\omega_x = 200/s$ on x -component for (a) baseline and (b) optimized flap

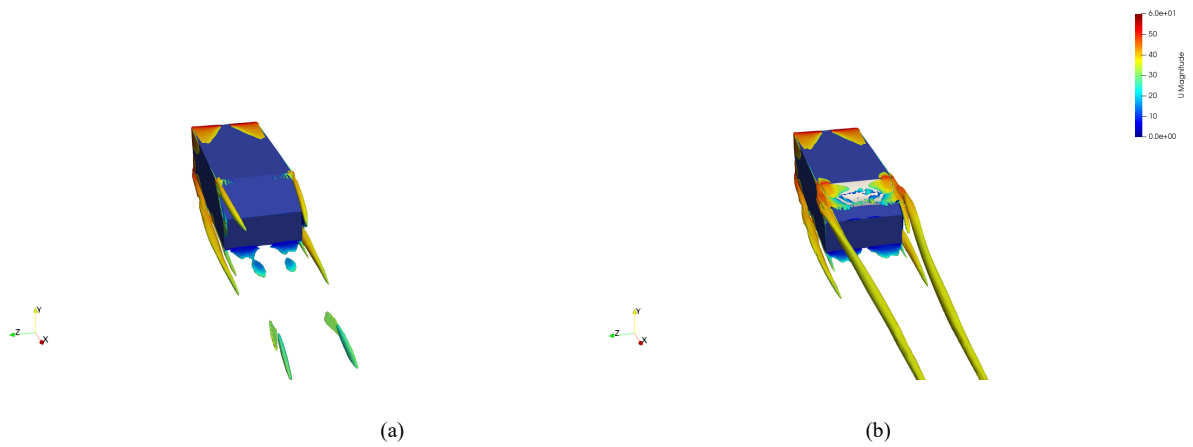


Figure 4.27 Contour plots for helicity $H = 7500m/s^2$ on x -component for (a) baseline and (b) optimized flap

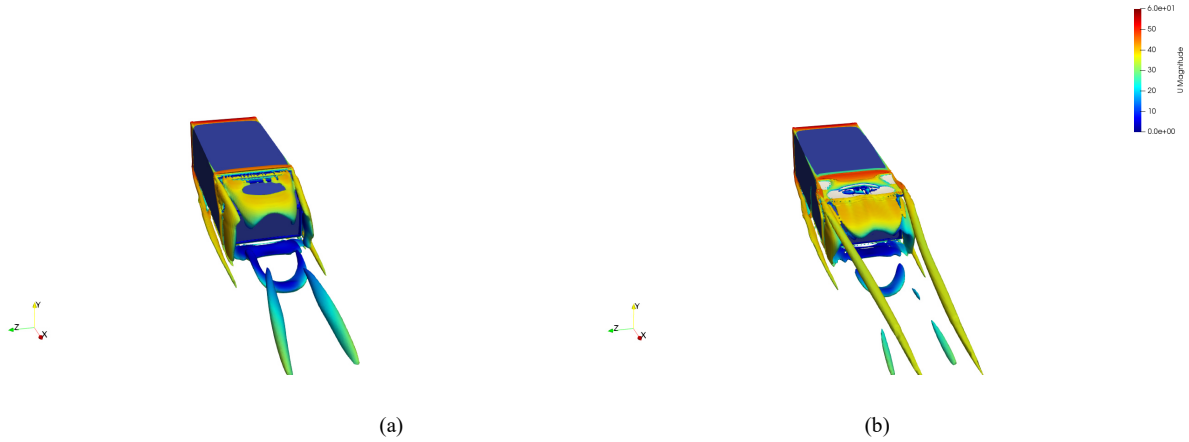


Figure 4.28 Contour plots for Q -criterion, where $Q/U_{ref}=150$ for (a) baseline and (b) optimized flap

Also, Figure 4.28 confirms the results of Figure 4.28. Lastly, Figure 4.29 also display the same behaviour, showing that the magnitude of the velocity in the y - z plane is stronger than the base case and also increased downstream. This again confirms the observation in Figure 4.27 to Figure 4.29.

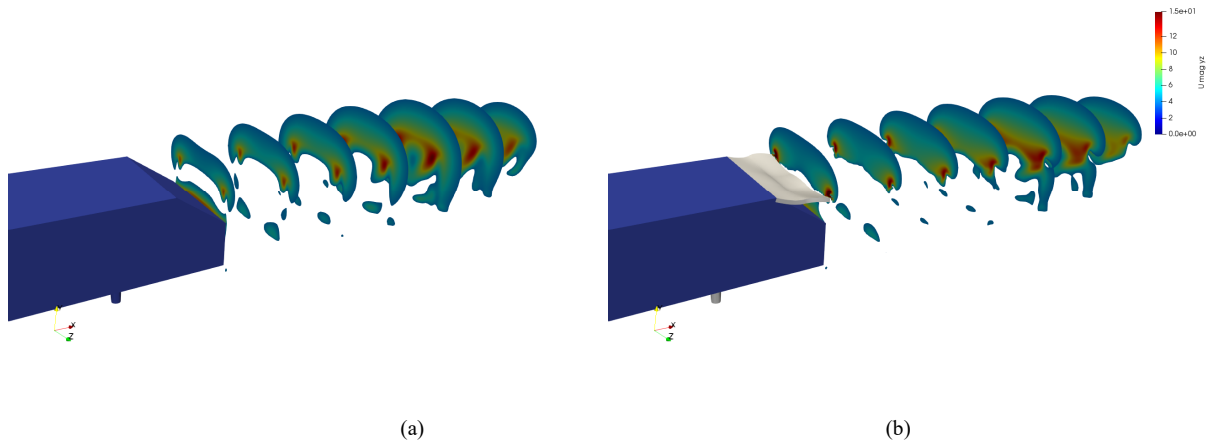


Figure 4.29 Velocity magnitude considering y - and z -components for (a) baseline and (b) optimized flap

Although the longitudinal vortices are usually not desirable features, they can reduce the size of the recirculation zone, as mentioned by Ehirim [33]. As a result, they can be used to reduce drag if properly controlled. It is based on this same principle that vortex generators used to create longitudinal vortices for drag reduction, as reported by Jean-Luc Aider [87]. Lastly, by reducing

the recirculation zone, it is believed that the soiling will be reduced. However, experimental data are needed for the validation of this concept.

Chapter 5 Concluding Remarks

5.1 Conclusion

This thesis has developed a method for genetic optimization of aerodynamic devices for road vehicle application. The method involves the integration of genetic algorithms, B-spline shape optimization and computational fluid dynamic using OpenFOAM. The method was successfully applied to generate unique device geometries based on the Ahmed body, which is a generic vehicle geometry. The following conclusions can be drawn from this study.

- Optimizing the flap for drag and downforce was effective. It reduced drag by 7.7% and increased downforce by 379.2%. The flap reduced the drag by reducing the longitudinal vortices and keeping the flow more attached to the Ahmed body. This caused the base pressure to increase. In addition, the downforce increased because the flap slowed down the flow and caused the pressure on top of it to increase.
- Optimizing the diffuser alone produced geometries that are consistent with previous studies. The diffuser reduced drag by 6.9% and lift by 2672.1%. This diffuser caused the flow to accelerate at the underbody side and also reduced the longitudinal vortices at the upper region of the wake. The combined effect caused drag and lift reduction.
- Optimizing the flap and diffuser together reduced the drag by 8.8% and lift by 2420.5%. Unexpectedly, the combined devices underperformed the individual diffuser in terms of downforce. This can be attributed to flow acceleration created by the combined flap/diffuser setup at the slant area of the rear, causing low pressure in that area, which adversely affected the downforce.
- Optimizing the flap for soiling and drag reduction generated stronger longitudinal

vortices but reduced the size of the recirculation zone. This caused an increase in pressure at the rear of the Ahmed body and reduced the drag by 10.4%.

5.2 Contribution

The main contribution of this thesis is the development of a novel method that combines B-spline surface optimization and a genetic algorithm in a 3D space for the optimization of aerodynamic devices for road vehicles. The method developed in this study allows the user to decide the specific aerodynamic device to optimize and the objective functions, and the algorithm can generate multiple non-intuitive and unique devices in a single run.

In addition, advanced vortex identification techniques were applied to the novel aerodynamic devices developed for the first time and provided physical insight into the drag and lift reduction as well as soiling mitigation mechanisms.

5.3 Future Work

Although the method developed has been demonstrated to be effective in generating unique and non-intuitive aerodynamic device geometries, it can still benefit from further improvements. The following ideas can be considered for future work.

- The method is computationally expensive at present and can be further optimized to improve the speed. This can be done by designating different core allocation to run individuals members of the population in parallel.
- There is a great opportunity to combine the adjoint method with genetic algorithms to produce a hybrid method that can outperform the adjoint method and the proposed method.

- Implement additional objectives functions for the soiling and test experimentally to assess which one produces better results.
- Implement the combinatorial problem that the algorithm will select the design of the devices and which device should be used. For example, if the user wants to use only one device, the algorithm will decide which one should be selected between the flap and diffuser.
- Include additional optimization algorithms to give the user the ability to select whichever is preferred, such as differential evolution, particle swap optimization and ant colony optimization.

References

- [1] F. Aqilah, M. Islam and F. Juretic, "CFD Analysis Around Ahmed Body Using A Laminar Kinetic," *Topical Problems of Fluid Mechanics*, pp. 1-8, 2019.
- [2] "Government of Canada," 12 April 2021. [Online]. Available: <https://www.canada.ca/en/environment-climate-change/services/climate-change/greenhouse-gas-emissions/sources-sinks-executive-summary-2021.html>. [Accessed 5 may 2021].
- [3] M. N. Sudin, M. A. Abdullah, S. A. Shamsuddin, F. R. Ramli and M. M. Tahir, "Review of Research on Vehicles Aerodynamic Drag Reduction Methods," *International Journal of Mechanical & Mechatronics Engineering*, vol. 14, no. 02, pp. 35-47, April 2014.
- [4] P. N. Krishnan and D. Zhou, "CFD Analysis of Drag Reduction for a Generic SUV," *ASME International Mechanical Engineering Congress and Exposition*, vol. 13, pp. 589-598, November 2009.
- [5] A. P. Gaylard, K. Kirwan and D. A. Lock, "Surface contamination of cars: A review," vol. 231, no. 9, pp. 1160-1176, August 2017.
- [6] H. Goetz, "The influence of wind tunnel tests on body design, ventilation, and surface deposits of sedans and sport cars.," *SAE Transactions*, vol. 80, pp. 854-872, January 1971.
- [7] S. Kajiwara, "Passive variable rear-wing aerodynamics of an open-wheel racing car," *Automotive and Engine Technology*, vol. 2, p. 107–117, August 2017.
- [8] M. Hammad, "Design and Analysis of Active Aerodynamic Control Systems for Increasing the Safety of High-Speed Road Vehicles," University of Ontario Institute of Technology, Oshawa, 2019.
- [9] G. K. W. Kenway, C. A. Mader, P. He and J. R. R. A. Martins, "Effective Adjoint Approaches for Computational Fluid Dynamics," *Progress in Aerospace Sciences*, vol. 110, no. 0376-0421, p. 100542, October 2019.
- [10] A. Hussain, Y. S. Muhammad, M. N. Saji, I. Hussain, A. M. Shoukry and S. Gani, "Genetic Algorithm for Traveling Salesman Problem with Modified Cycle Crossover Operator," *Computational Intelligence and Neuroscience*, vol. 2017, p. 7, 2017.

- [11] X. S. Yang, "Optimization and Metaheuristic Algorithms in Engineering," *Metaheuristics in Water, Geotechnical and Transport Engineering*, pp. 1-23, 2013.
- [12] F. Muyl, L. Dumas and V. Herbert, "Hybrid method for aerodynamic shape optimization in automotive industry," *Computers & Fluids*, vol. 33, no. 5-6, pp. 849-858, July 2004.
- [13] J. Doyle, R. Hartfield and C. Roy, "Aerodynamic Optimization for Freight Trucks using a Genetic Algorithm and CFD," *Aerospace Sciences Meeting and Exhibit*, vol. 46, June 2008.
- [14] S. Phadte, "Vehicle layout optimization using multi-objective genetic algorithms," *2017 International Conference on Algorithms, Methodology, Models and Applications in Emerging Technologies*, pp. 1-10, 2017.
- [15] Z. M. Saleh, A. H. Ali and M. S. Abood, "Drag Reduction Using Passive Methods on KIA PRIDE Car Model," *Journal of Engineering*, vol. 26, pp. 47-63, April 2020.
- [16] R. B. Bansal and R. B. Sharma, "Drag Reduction of Passenger Car Using Add-On Devices," *Journal of Aerodynamics*, vol. 2014, p. 13, March 2014.
- [17] S. M. R. Hassan, T. Islam, M. Ali and M. QuamrulIslam, "Numerical Study on Aerodynamic Drag Reduction of Racing Cars," *Procedia Engineering*, vol. 90, pp. 308-313, December 2014.
- [18] N. A. Siddiqui and M. Agelin-Chaab, "A Simple Passive Device for the Drag Reduction of an Ahmed Body," *Journal of Applied Fluid Mechanics*, vol. 14, pp. 147-164, January 2021.
- [19] J. Muñoz-Paniagua, J. García and A. Crespo, "Aerodynamic optimization of high-speed trains nose using a genetic algorithm and artificial neural networks," *An ECCOMAS Thematic Conference*, 2011.
- [20] C. Liu, W. Bu and D. Xu, "Multi-objective shape optimization of a plate-fin heat exchanger using CFD and multi-objective genetic algorithm," *International Journal of Heat and Mass Transfer*, vol. 111, pp. 65-82, August 2017.
- [21] W. Hucho and G. Sovran, "Aerodynamics of road vehicles," *Annual Review of Fluid Mechanics*, vol. 25, pp. 485-537, 1993.

- [22] J. E. Hesselgreaves, R. Law and D. A. Reay, "Chapter 5 - Aspects of Flow and Convective Heat Transfer Fundamentals for Compact Surfaces," in *Compact Heat Exchangers*, Butterworth-Heinemann, 2017, pp. 157-219.
- [23] P. K. Chang, "CHAPTER XII - Control of Separation of Flow," in *Separation of Flow*, Pergamon, 1970, pp. 716-752.
- [24] D. S. Nath, P. C. Pujari and A. Jain, "Drag reduction by application of aerodynamic devices in a race car," *Advances in Aerodynamics*, vol. 3, January 2021.
- [25] B. Khalighi, K. Chen and G. Iaccarino, "Study of Drag Reduction Devices for a Square Back Vehicle Configuration Using," *Proceedings of the ASME 2012 Fluids Engineering Summer Meeting*, vol. 1, pp. 1-8, July 2012.
- [26] T. Skrucany , B. Sarkan and J. Gnap , "Influence of Aerodynamic Trailer Devices," *Eksploatacja i Niezawodnosc – Maintenance and Reliability*, vol. 18, p. 151–154, 2016.
- [27] M. Khosravi, F. Mosaddeghi and M. Oveisi, "Aerodynamic drag reduction of heavy vehicles using append devices by CFD analysis," *Journal of Central South University*, vol. 22, p. 4645–4652, December 2015.
- [28] T. Charles, Z. Yang and Y. Lu, "Assessment of Drag Reduction Devices Mounted on a Simplified Tractor," *Journal of Applied and Computational Mechanics*, vol. 7, no. 2383-4536, pp. 45-53, 2021.
- [29] J. F. Beaudoin, and J. L. Aider, "Drag and lift reduction of a 3D bluff body using flaps," *Experiments in Fluids*, vol. 44, pp. 491-501, February 2008.
- [30] G. Fourrié, L. Keirsbulck, L. Labraga and P. Gilliéron, "Bluff-body drag reduction using a deflector," *Experiments in Fluids*, vol. 50, pp. 385-395, July 2010.
- [31] J. Tian, Y. Zhang, H. Zhu and H. Xiao, "Aerodynamic drag reduction and flow control of Ahmed body with flaps," *Advances in Mechanical Engineering*, vol. 9, no. 7, pp. 1-17, July 2017.
- [32] A. Altaf, A. A. Omar and W. Asrar, "Passive drag reduction of square back road vehicles," *Journal of Wind Engineering and Industrial Aerodynamics*, vol. 134, pp. 30-43, November 2014.

- [33] O. H. Ehirim, K. Knowles, A. J. Saddington and M. V. Finnis, "Aerodynamics of a Convex Bump on a Ground-Effect Diffuser," *Journal of Fluids Engineering*, vol. 140, September 2018.
- [34] L. Jowsey and M. Passmore, "Experimental Study of Multiple-Channel Automotive Underbody Diffusers," *Journal Automobile Engineering*, vol. 224, no. 7, May 2010.
- [35] L. Jowsey, "An Experimental Study of Automotive Underbody Diffusers," Loughborough University, 2013.
- [36] P. Salhan, "Computational Study of the Front-end Downforce Enhancing Aerodynamic Elements in Sports Cars," 2020.
- [37] E. M. Papoutsis-Kiachagias, V. G. Asouti, and K. C. Giannakoglou, "Multi-point aerodynamic shape optimization of cars based on continuous adjoint," *Structural and Multidisciplinary Optimization*, vol. 59, p. 675–694, February 2019.
- [38] M. Ebrahimi and A. Jahangirian, "Aerodynamic Optimization of Airfoils Using Adaptive Parameterization and Genetic Algorithm," *Journal of Optimization Theory and Applications*, vol. 162, p. 257–271, October 2013.
- [39] A. Dina, S. Danaila, M.-V. Pricop and I. Bunesco, "Using genetic algorithms to optimize airfoils in incompressible regime," *INCAS BULLETIN*, vol. 11, no. 1, pp. 79-90, 2019.
- [40] V. Nejati and K. Matsuuchi, "Aerodynamics Design and Genetic Algorithms for Optimization of Airship Bodies," *JSME International Journal Series B*, vol. 46, no. 4, pp. 610-617, 2003.
- [41] J. J. Hernández, E. Gómez, J. I. Grageda, C. Couder, A. Solís, C. L. Hanotel and J. I. Ledesma, "Evolving aerodynamic airfoils for wind turbines through a genetic algorithm," *Journal of Physics: Conference Series*, vol. 792, p. 012079, January 2017.
- [42] A. Gehrke, G. De Guyon-Crozier and K. Mulleners, "Genetic Algorithm Based Optimization of Wing Rotation in Hover," *Fluids*, vol. 3, no. 3, pp. 59-67, August 2018.
- [43] I. Cayiroglua and R. Kilicb, "Wing Aerodynamic Optimization by Using Genetic Algorithm and Ansys," *Acta Physica Polonica Series A*, vol. 132, pp. 981-985, September 2017.
- [44] D. Sasaki, M. Morikawa, S. Obayashi and K. Nakahashi, "Aerodynamic Shape Optimization

- of Supersonic Wings by Adaptive Range Multiobjective Genetic Algorithms," *Evolutionary Multi-Criterion Optimization.*, vol. 1993, pp. 639-652, July 2001.
- [45] R. A. E. Mäkinen, J. Periaux and J. Toivanen, "Multidisciplinary Shape Optimization in Aerodynamics and Electromagnetics using Genetic Algorithms," *International Journal for Numerical Methods in Fluids*, vol. 30, p. 149–159, May 1999.
- [46] C. Y. Yuan and M. Q. Li, "Multi-objective optimization for the aerodynamic noise of the high-speed train in the near and far field based on the improved NSGA-II algorithm," *Journal of Vibroengineering*, vol. 19, no. 6, pp. 4759-4782, September 2017.
- [47] M. G. Yu, J. Y. Zhang and W. H. Zhang, "Multi-objective optimization design method of the high-speed train head," *Journal of Zhejiang University SCIENCE A*, vol. 14, p. 631–641, September 2013.
- [48] Y. Yusoff, M. S. Ngadiman and A. M. Zain, "Overview of NSGA-II for Optimizing Machining Process Parameters," *Procedia Engineering*, vol. 15, pp. 3978-3983, December 2011.
- [49] P. Bearman and D. Trueman, "An investigation of the flow around rectangular cylinders," *Aeronautical Quarterly*, vol. 23, pp. 229-237, August 1972.
- [50] O. Mizota and A. Okajima, "Experimental Studies of Time Mean Flows Around Rectangular Prisms," *Proceedings of the Japan Society of Civil Engineers*, vol. 1981, no. 312, pp. 39-47, 1981.
- [51] . M. Matsumoto, "Vortex Shedding of Bluff Bodies: A Review," *Journal of Fluids and Structures*, vol. 13, no. 7–8, pp. 791-811, October 1999.
- [52] Leclercq, D. J. J. Leclercq and C. J. Doolan, "The interaction of a bluff body with a vortex wake," *Journal of Fluids and Structures*, vol. 25, no. 5, pp. 867-888, July 2009.
- [53] J. A. Fitzpatrick, "Flow/acoustic interactions of two cylinders in cross-flow," *Journal of Fluids and Structures*, vol. 17, no. 1, pp. 97-113, January 2003.
- [54] V. Holmen, "Methods for Vortex Identification," 2012.
- [55] C. Liu, Y. Gao and X. Dong, "Third generation of vortex identification methods: Omega and Liutex/Rortex based systems," *Journal of Hydrodynamics volume*, vol. 31, p. 205–223,

February 2019.

- [56] J. Jilesen, A. Gaylard, and J. Escobar, "Numerical Investigation of Features Affecting Rear and Side Body Soiling," *SAE International Journal of Passenger Cars*, vol. 10, no. 1, pp. 299-308, 2017.
- [57] M. Yoshida, A. Yamatani and H. China, "Prediction of dirt contamination on vehicle body surface," *JSAE Review*, vol. 19, no. 3, pp. 257-262, July 1998.
- [58] S. Roettger, M. Schulz, W. Bartelheimer and T. Ertl, "Automotive Soiling Simulation Based On Massive Particle Tracing," *Data Visualization*, pp. 309-317, 2001.
- [59] S. Roettger, T. Ertl, M. Schulz and W. Bartelheimer, "Flow Visualization on Hierarchical Cartesian Grids," *High Performance Scientific And Engineering Computing*, vol. 21, pp. 139-146, 2002.
- [60] J. Paschkewitz, "Simulation of spray dispersion in a simplified heavy vehicle wake," January 2006.
- [61] J. S. Paschkewitz, "A comparison of dispersion calculations in bluff body wakes using LES and unsteady RANS," 2006.
- [62] T. Kuthada and S. Cyr, "Approaches to Vehicle Soiling," in *Progress in Vehicle Aerodynamics*, "4th FKFS conference on progress in vehicle aerodynamics and thermal management: numerical methods (eds Wiedermann, J, Hucho, WH), Stuttgart, Germany, p. 111–123, 2006.
- [63] . I. Spruss, T. Kuthada, J. Wiedemann, S. Cyr and B. Duncan, "Spray Pattern of a Free Rotating Wheel: CFD Simulation and Validation," *Progress in Vehicle Aerodynamics and Thermal Management*, p. 64–80, 2011.
- [64] A. P. Gaylard and B. Duncan, "Simulation of Rear Glass and Body Side Vehicle Soiling by Road Sprays," *SAE International Journal of Passenger Cars*, vol. 4, no. 1, pp. 184-196, November 2016.
- [65] . P. Elofsson and M. Bannister, "Drag Reduction Mechanisms Due to Moving Ground and Wheel Rotation in Passenger Cars," *SAE Technical Paper 2002-01-0531*, March 2002.
- [66] A. Kabanovs, M. Varney, A. Garmory and M. Passmore, "Experimental and Computational

- Study of Vehicle Surface Contamination on a Generic Bluff Body," *SAE Technical Paper 2016-01-1604*, p. 13, 2016.
- [67] D. Cappelli and N. N. Mansour, "Performance of Reynolds Averaged Navier-Stokes Models in Predicting Separated Flows: Study of the Hump Flow Model Problem," *AIAA Applied Aerodynamics Conference*, vol. 4, pp. 2869-2894, 2013.
- [68] G. Boudier, L. Y. M. Gicquel, T. Poinso, D. Bissières and C. Bérat, "Comparison of LES, RANS and experiments in an aeronautical gas turbine combustion chamber," *Proceedings of the Combustion Institute*, vol. 31, no. 2, pp. 3075-3082, January 2007.
- [69] Y. Tominaga and T. Stathopoulos, "CFD modeling of pollution dispersion in a street canyon: Comparison between LES and RANS.," *Journal of Wind Engineering and Industrial Aerodynamics*, vol. 99, no. 4, pp. 340-348, April 2011.
- [70] Y. Tominaga and T. Stathopoulos, "Numerical simulation of dispersion around an isolated cubic building: Model evaluation of RANS and LES.," *Building and Environment*, vol. 45, no. 10, pp. 2231-2239, October 2010.
- [71] S. M. Salim, R. Buccolieri, A. Chan and S. D. Sabatino, "Numerical simulation of atmospheric pollutant dispersion in an urban street canyon: Comparison between RANS and LES," *Journal of Wind Engineering and Industrial Aerodynamics*, vol. 99, no. 2-3, pp. 103-113, March 2011.
- [72] D. C. A. MONK, "Comparison of Turbulence Models Effectiveness for a Delta Wing at Low Reynolds Numbers."
- [73] D. Igali, O. Mukhmetov and Y. Zhao, "Comparative Analysis of Turbulence Models for Automotive Aerodynamic Simulation and Design.," *International Journal of Automotive Technology*, vol. 20, p. 1145-1152, September 2019.
- [74] Ansys Inc, "Ansys User Guide," November 2013.
- [75] B. Nebenfuhr, "OpenFOAM: A tool for predicting automotive relevant flow fields," Chalmers University of Technology, Goteborg, 2010.
- [76] E. Robertson, V. Choudhury, S. Bhushan and D. K. Walte, "Validation of OpenFOAM numerical methods and turbulence models for incompressible," *Computers & Fluids*, vol. 123, pp. 122-145, December 2015.

- [77] OpenFOAM, "User Guide OpenFOAM".
- [78] W. Meile, T. Ladinek, G. Brenn, A. Reppenhagen and A. Fuchs, "Non-symmetric bi-stable flow around the Ahmed body,," *International Journal of Heat and Fluid Flow*, vol. 57, pp. 34-47, 2016.
- [79] H. Lienhart, S. Becker and C. Stoots, "Flow Around a Simplified Car," European research community on flow turbulence and combustion, 2000. [Online]. Available: [http://cfd.mace.manchester.ac.uk/ercoftac/doku.php?id=cases:case082&s\[\]=ahmed&s\[\]=body](http://cfd.mace.manchester.ac.uk/ercoftac/doku.php?id=cases:case082&s[]=ahmed&s[]=body). [Accessed 5 May 2021].
- [80] S. Ahmed, G. Ramm and G. Faltin, "Some Salient Features Of The Time-Averaged Ground Vehicle Wake," *SAE Technical Paper 840300*, 1984.
- [81] W. Meile, G. Brenn, A. Reppenhagen, B. Lechner and A. Fuchs, "Experiments and numerical simulations on the aerodynamics of the Ahmed body," *CFD Letters*, vol. 2, pp. 32-39, March 2011.
- [82] V. Jain, G. Sachdeva, S. S. Kachhwaha and B. Patel, "Thermo-economic and environmental analyses based multi-objective optimization of vapor compression-absorption cascaded refrigeration system using NSGA-II technique," *Energy Conversion and Management*, vol. 113, pp. 230-242, April 2016.
- [83] D. Kalyanmoy, *Multi-Objective Optimization Using Genetic Algorithms*, 2001.
- [84] E.-G. Talbi, *Metaheuristics: From Design to Implementation*, 2009.
- [85] X.-S. Yang, M. Karamanoglu and X. He, "Multi-Objective Flower Algorithm for Optimization," *Procedia Computer Science*, vol. 18, pp. 861-868, 2013.
- [86] N. M. Patrikalakis, T. Maekawa and W. Cho, "Shape Interrogation for Computer Aided Design and Manufacturing," December 2009. [Online]. Available: <https://web.mit.edu/hyperbook/Patrikalakis-Maekawa-Cho/>. [Accessed 6 May 2021].
- [87] J. L. Aider, J. F. Beaudoin and J. E. Wesfreid, "Drag and lift reduction of a 3D bluff-body using active vortex," *Experiments in Fluids*, vol. 48, p. 771–789, October 2009.
- [88] F. Delassaux, "Sensitivity analysis of hybrid methods for the flow around the Ahmed body

with application to passive control with rounded edges," *Computers & Fluids*, vol. 214, January 2021.

- [89] H. Viswanathan, "Aerodynamic performance of several passive vortex generator configurations on an Ahmed body subjected to yaw angles," *Journal of the Brazilian Society of Mechanical Sciences and Engineering*, vol. 43, February 2021.
- [90] P. Moghimi and R. Rafee, "Numerical and Experimental Investigations on Aerodynamic Behavior of the Ahmed Body Model with Different Diffuser Angles," *Journal of Applied Fluid Mechanics*, vol. 11, pp. 1101-1113, July 2018.
- [91] A. R. George and J. E. Donis, "Flow patterns, pressures and forces on the underside of idealised ground effect vehicles.," *Aerodynamics of Transportation*, vol. 7, pp. 69-79, 1983.
- [92] X. Zhang, A. Senior and A. Ruhrmann, "Vortices behind a bluff body with an upswept aft section in ground effect.," *International Journal of Heat and Fluid Flow*, vol. 25, no. 1, pp. 1-9, February 2004.